# Dynamics of the solar chromosphere

## III. Ultraviolet brightness oscillations from TRACE

J. M. Krijger[1], R. J. Rutten[1], B. W. Lites[2], Th. Straus[3], R. A. Shine[4], and T. D. Tarbell[4]

[1] Sterrekundig Instituut, Postbus 80 000, 3508 TA Utrecht, The Netherlands
   e-mail: J.M.Krijger@astro.uu.nl, R.J.Rutten@astro.uu.nl
[2] High Altitude Observatory, National Center for Atmospheric Research, PO Box 3000,
   Boulder CO 80307-3000, USA
   e-mail: lites@hao.ucar.edu
[3] Osservatorio Astronomico di Capodimonte, Via Moiariello 16, 80131 Napoli, Italy
   e-mail: straus@na.astro.it
[4] Lockheed Martin Solar and Astrophysics Lab, Dept. L9–41, Building 252, 3251 Hanover Street, Palo Alto,
   CA 94304, USA
   e-mail: shine@lmsal.com; tarbell@lmsal.com

**Abstract.** We analyze oscillations in the solar atmosphere using image sequences from the *Transition Region and Coronal Explorer* (TRACE) in three ultraviolet passbands which sample the upper solar photosphere and low chromosphere. We exploit the absence of atmospheric seeing in TRACE data to furnish comprehensive Fourier diagnostics (amplitude maps, phase-difference spectra, spatio-temporal decomposition) for quiet-Sun network and internetwork areas with excellent sampling statistics. Comparison displays from the ground-based Ca II H spectrometry that was numerically reproduced by Carlsson & Stein are added to link our results to the acoustic shock dynamics in this simulation. The TRACE image sequences confirm the dichotomy in oscillatory behaviour between network and internetwork and show upward propagation above the cutoff frequency, the onset of acoustic shock formation in the upper photosphere, phase-difference contrast between pseudo-mode ridges and the inter-ridge background, enhanced three-minute modulation aureoles around network patches, a persistent low-intensity background pattern largely made up of internal gravity waves, ubiquitous magnetic flashers, and low-lying magnetic canopies with much low-frequency modulation. The spatio-temporal occurrence pattern of internetwork grains is found to be dominated by acoustic and gravity wave interference. We find no sign of the high-frequency sound waves that have been proposed to heat the quiet chromosphere, but such measurement is hampered by non-simultaneous imaging in different passbands. We also find no signature of particular low-frequency fluxtube waves that have been proposed to heat the network. However, internal gravity waves may play a role in their excitation.

**Key words.** Sun: photosphere – Sun: chromosphere – Sun: oscillations

## 1. Introduction

This paper addresses oscillations of the quiet solar atmosphere from image sequences taken with the *Transition Region and Coronal Explorer* (TRACE). TRACE images the Sun from a Sun-synchronous orbit at characteristic temperatures between $10^4$ K and $10^7$ K by sequentially selecting different spectral passbands to feed a $1024 \times 1024$ px$^2$ CCD camera with 0.5 arcsec pixels (366 km/px on the Sun) that covers nearly 10% of the solar disk. Details are given by Handy et al. (1999). First results from the spectacular coronal movies taken through

the TRACE far-ultraviolet passbands were presented by Schrijver et al. (1999).

In this paper we use image sequences taken through the ultraviolet TRACE passbands centered at $\lambda = 1700$, 1600, and 1550 Å to study quiet-Sun oscillations in the upper photosphere and low chromosphere. We so return to the domain of the pioneering rocket studies of 1600 Å "cell grains" by Brueckner (1980) and Cook et al. (1983) using the HRTS rocket spectrograph, and by Bonnet et al. (1982), Foing & Bonnet (1984a,b), Foing et al. (1986), and Damé et al. (1986) using the TRC rocket filtergraph. The obvious improvement that TRACE brings over the TRC flights is enormous sequence duration increase and digital data registration per CCD instead of emulsion.

TRACE has no spectrograph so that emulation of the HRTS flights requires multi-spacecraft campaigns as in the recent TRACE-plus-SUMER (and MDI) analysis of Judge et al. (2001). The strength of the present analysis is the large statistical significance offered by TRACE image sequences and the use of comprehensive and complementary Fourier diagnostics to provide a complete inventory.

In standard models of the solar atmosphere such as VAL-C of Vernazza et al. (1973, 1976, 1981) and FAL-C of Fontenla et al. (1993), the disk-center intensity at 1700 Å emerges from the "upper photosphere", 1550 Å radiation from the "lower chromosphere", and 1600 Å radiation from the "temperature minimum region", where the temperature minimum at $h = 500$ km above continuum optical depth $\tau_5 = 1$ at $\lambda = 5000$ Å defines the transition from photosphere to chromosphere (see the formation panels in Fig. 36 of Vernazza et al. 1981). The ubiquitous existence of a chromospheric temperature rise in shell-like ("plane-parallel") stratification over $h = 500-1000$ km is presently in debate on the basis of the very oscillations discussed here and reviewed below, but we maintain this nomenclature for clarity. Also, we prefer to use "chromospheric dynamics" even for the upper-photosphere diagnostics since the TRACE UV passbands essentially sample the onset of chromospheric oscillations and the chromospheric network.

The same atmospheric regime is accessible to ground-based observation and has been studied extensively using the cores of strong absorption lines and the Ca II $K_{2V}$ and $H_{2V}$ inner-wing reversals. Although TRACE does not reach the angular resolution of ground-based telescopes at good seeing, TRACE image sequences offer the important advantage of distortion-free sampling over relatively long duration. Compared with oscillation studies employing Fraunhofer line spectrometry in the visible to probe these and lower heights in the solar atmosphere or ultraviolet line spectrometry to probe greater heights, the lack of Dopplershift information is a disadvantage, but TRACE imaging yields data from a far larger area than is sampled by a spectrograph slit and so permits a much more complete view of solar variations as well as much better statistical reliability in their diagnosis. In addition, the wide-band continua sampled by the TRACE 1700 and 1600 Å passbands do not suffer Dopplershift contamination as is the case for the apparent brightness modulation of optically thick lines (including the inner wings of Ca II H & K, see Sect. 4.3). These outstanding TRACE capabilities are exploited here to wrap up much previous work.

The extensive older literature on oscillations in the upper photosphere and lower chromosphere has been reviewed by Rutten & Uitenbroek (1991a); more recent work is reviewed by Rutten (1994, 1995, 1999, 2001). Stein & Carlsson (1997), Carlsson & Stein (1998), Carlsson (1999), Deubner (1998), and Deubner & Steffens (1999). Even in quiet-Sun areas strict distinction must be made between network and internetwork. The first term denotes those parts of the supergranular cell boundaries that contain kiloGauss magnetic elements at sufficient spatial density

to show up on photospheric magnetograms and on chromospheric images taken in the core of Ca II K or the ultraviolet TRACE passbands. On such filtergrams the chromospheric network appears as chains of bright patches, each corresponding to a cluster of thin magnetic elements in the underlying photosphere. The latter, commonly identified with the modeller's fluxtubes, make up the magnetic network and may appear as individual bright grains in high-resolution (better than 0.5 arcsec) movies made in the Fraunhofer G band around $\lambda = 430.5$ Å (e.g., Muller et al. 1989; Title & Berger 1996; Berger et al. 1998; movies on the Dutch Open Telescope website (URL http://dot.astro.uu.nl).

The bright patches on chromospheric filtergrams map the supergranular cell boundaries too sparsely to make the network identifiable as cellular patterning on snapshot images (cf. Hagenaar et al. 1997), but they stand out in longer-duration image sequences by being generally brighter and much more stably present than the transient, often briefly repetitive and often fast-moving, grainy brightness features seen in the intervening "internetwork" areas corresponding to supergranular cell interiors.

The high degree of cospatiality of the brightness features seen in Ca II K and the TRACE ultraviolet channels has been demonstrated by Rutten et al. (1999a). The correspondence between network grains in Ca II K and clusters of smaller G-band magnetic elements located in underlying intergranular lanes is illustrated in Fig. 2 of Lites et al. (1999). The dynamical behaviour of the Ca II K internetwork brightness patterning is illustrated in Fig. 3 of the same paper. Figure 5 of Rutten et al. (1999b) illustrates similar behaviour in a TRACE 1550 Å image sequence. Figure 5 below shows a comparable 1700 Å sequence.

The internetwork "three-minute" oscillations (often in their "internetwork grain" disguise and often called "$K_{2V}$ grains", see Rutten & Uitenbroek 1991a) are intensely discussed in the recent literature after their identification as weak acoustic shocks by Carlsson & Stein (1992, 1994, 1995, 1997, 1998). Major issues that are presently in debate are, respectively: (i) – the degree of correlation between internetwork grain occurrence and enhanced internetwork field (Lites et al. 1999 and references therein; Worden et al. 1999), (ii) – the presence of identifiable pistons at or below the surface that cause enhanced acoustic flux higher up in the atmosphere (Hoekzema & Rutten 1998; Hoekzema et al. 1998a; Hoekzema & Brandt 2000; Kiefer & Balthasar 1998; Goode et al. 1998; Skartlien 1998; Rast 1999; Skartlien et al. 2000), (iii) – the relation between such pistons and observed velocity-intensity ($V-I$) phase-difference patterns in photospheric $(k, \omega)$ diagrams (Straus et al. 1999; Oliviero et al. 1999; Skartlien & Rast 2000) with additional interest concerning $p$-mode asymmetries (Nigam & Kosovichev 1999a, 1999b; Georgobiani et al. 2000), (iv) – the amount of wave reflection in the upper chromosphere (Deubner et al. 1992, 1996; Kneer & von Uexküll 1993; von Uexküll & Kneer 1995; Jefferies et al. 1997; Schmitz & Steffens 1999; Carlsson & Stein 1999), (v) – the penetration height of the shocks

into the higher chromosphere as evidenced by ultraviolet spectrometry with HRTS (Hoekzema et al. 1997) and SUMER (Steffens et al. 1997; Carlsson et al. 1997, 1999; Curdt & Heinzel 1998; Gouttebroze et al. 1999; Doyle et al. 1999; Curdt et al. 1999; Carlsson 1999; Wikstøl et al. 2000; Judge et al. 2001), *(vi)* – the shock contribution to chromospheric heating (Theurer et al. 1997a, 1997b; Kalkofen et al. 1999), *(vii)* – the shock contribution to the basal flux observed from cool stars (Cuntz et al. 1999; cf. Ulmschneider 1999), and *(viii)* – the shock contribution to the FIP split affecting solar wind abundances (Rutten 1997; Judge & Peter 1998). Our TRACE results displayed below bear, directly or indirectly, on all these internetwork debates.

Network oscillations are often invoked to supply chromospheric or coronal heating, but there is no firm identification yet nor have they so far benefited from detailed observation modelling comparable to the Carlsson–Stein internetwork shock simulation. No high-frequency modes have been identified. Well-established (and often rediscovered) dichotomies are that the chromospheric network brightness modulation differs distinctly from the internetwork in showing primarily periodicities of $P \approx$ 5 min and longer, and that these modulations are much clearer in Dopplershift than in brightness (e.g., Jensen & Orrall 1963; Liu & Sheeley 1971; Cram 1978; Lites et al. 1993). Kneer & Von Uexküll (1985, 1986) have suggested that the observed slow periodicities represent erratic fluxtube footpoint motions whereas Kalkofen (1997, 1999) argues that they are magnetoacoustic modes that are generated impulsively as transverse waves in the photosphere and become longitudinal higher up, and Goodman (2000) proposes that linear fluxtube waves drive transverse charged-particle currents which provide heating by resistive dissipation. An additional network issue is posed by the three-minute "power aureoles" around dense network and plage (Braun et al. 1992; Brown et al. 1992; Toner & LaBonte 1991; Hindman & Brown 1998; Braun & Lindsey 1999), and the reversed-sign "power shadows" found by Judge et al. (2001). We address the network issues below as well.

This paper is an initial TRACE study of oscillations in the quiet-Sun temperature-minimum domain. Our goal is to provide a comprehensive inventory and to place that in the context summarised above, combining standard oscillation analysis techniques with a variety of display formats: *(i)* – space-time displays plotting spatial development patterns; *(ii)* – power-map displays plotting Fourier amplitude per spatial element and per temporal frequency bin; *(iii)* – one-dimensional Fourier spectra of oscillatory power, phase difference and phase coherence, with separation of the network and internetwork contributions, and *(iv)* – two-dimensional $(k_h, f)$ phase-difference spectra. These displays represent a space-based counterpart to the similar ones from ground-based filtergram sequences in Kneer & von Uexküll (1993). It is worthwhile to combine these different formats in a single paper to enable interpretative comparisons, but the disadvantage is that the interpretation ranges widely, from acoustic to gravity to canopy waves.

We also add pertinent comparison displays of the Ca II H spectrogram sequences that were used by Lites et al. (1993, henceforth Paper I) to describe chromospheric network oscillations in the first paper of this series. The internetwork part of these sequences provided both the photospheric input and the chromospheric testing ground for the numerical simulations of Carlsson & Stein (1997, henceforth CS1997). These data merit a revisit here in order to link our TRACE results to this numerical modelling and to the properties of the same oscillations when sampled by the Ca II H core and wings.

The organization of the paper is as follows. The observations are presented in the next section. Section 3 defines our Fourier methods. In Sect. 4 we display TRACE results from May 12, 1998 together with Ca II H comparisons in the various graphical forms listed above. We add an extensive error analysis in Sect. 5, including comparison with an independent TRACE data set from October 14, 1998. Some results are discussed in the context of other work in Sect. 6. The conclusions follow in Sect. 7.

## 2. Observations and reduction

TRACE sequences. We use two different TRACE data sequences in this paper, from May 12, 1998 and October 14, 1998, respectively. Both were downloaded from the public TRACE archive (URL http://vestige.lmsal.com/TRACE/). Details are given in Table 1; background information is available in the TRACE Analysis Guide (URL http://diapason.lmsal.com/~bentley/guides/tag/). During the first run (which was part of Joint Observing Program JOP72 in which most of us participated) TRACE was programmed to observe a rectangular quiet region near disk center sequentially in its three ultraviolet passbands. In the second run, TRACE observed an even quieter rectangular disk-center area with broad-band white light imaging added into the passband sequence. The white light images show (but do not resolve) the solar granulation. They are not used in this paper but may serve for photospheric piston searches in future analyses.

Following the TRACE Analysis Guide we subtracted the readout pedestal of 86 readout units from the images for the 12 May data. We did not apply flat-field corrections or bad-pixel eliminations since none are specified for this date. For the 14 Oct. data we used the nominal dark field and the flat field measured on 31 August. The top and bottom pixel rows of the May 12 images are very noisy and were discarded. Only two frames in each data set were affected by telemetry errors; they were replaced by the averages of the preceding and subsequent images. Minor effects from the data compression appear in the data, for example as a low-amplitude interference pattern in spatial frequency in Fig. 23.

**Table 1.** TRACE observations used in this paper.

| date | May 12, 1998 | October 14, 1998 |
|---|---|---|
| program sequence | TDT.trnotsofast | TDT.any_frames |
| image size [px] | $256 \times 1024$ | $512 \times 512$ |
| number of images | 354 | 612 |
| $X_{\rm cen}, Y_{\rm cen}$ [arcsec] | $-40, 308$ | $-13, -82$ |
| $L_{\rm cen}, B_{\rm cen}$ [deg] | $-2.51, 15.98$ | $-0.77, 1.04$ |
| duration [UT] | 14:30–16:00 | 08:12–12:00 |
| cadence [s] | 15.0573 | 21.8625 |
| exposure 1700 Å [s] | 2.0479 | 2.0480 |
| exposure 1600 Å [s] | 1.0239 | 1.0239 |
| exposure 1550 Å [s] | 5.7919 | 9.7400 |
| exposure white [s] | — | 0.0064 |



**Fig. 1.** Solar location of the fields observed with TRACE on May 12, 1998 (left) and October 14, 1998 (right). The grid shows heliocentric longitude and latitude for each date.

Passbands. Transmission curves for the three ultraviolet passbands are given by Handy et al. (1998) together with a numerical recipe to isolate the contribution of the C IV doublet at $\lambda = 1548$ Å and 1550 Å through optimised combination of images taken in the three ultraviolet passbands. The C IV lines dominate the 1550 Å brightness in active areas, but in quiet areas contributions from C I lines, from other lines, and from the continuum dominate in the 20 Å wide 1550 Å passband. We display Fourier results for such C IV "constructs" below in which the combination recipe was applied to the Fourier transforms of the three sequences, after Fourier demodulation to correct for the time delays between the sequentially exposed images.

Exposure timing. The TRACE housekeeping data specify the exposure duration and the moment at which the shutter closed for each individual image. The nominal delay between successive images in a given passband was 15 s for May 12 and 21 s for October 14. Occasionally there were 1 s longer intervals on May 12 and up to 10 s longer intervals on Oct. 14; the cadence values in Table 1 are sequence averages. These erratic increments upset the use of standard Fast Fourier Transform (FFT) routines which assume equidistant spacing. We therefore defined an equidistant time scale for each dataset, combining the average interval with an optimum starting time, and then selected the image closest to each equidistant time step for FFT analysis. For the May 12 data, the offset from the actual mid-exposure time is always shorter than half the exposure duration. The slower cadence and longer 1550 Å exposures of the October 14 data combine into larger offsets. However, worse effects result from the non-simultaneity of the imaging in the different passbands (Sect. 6).

Observed fields. The $(X_{\rm cen}, Y_{\rm cen})$ values in Table 1 specify the location of the center of the field in the TRACE coordinate system measuring distance from apparent disk center in arcsec on the sky along the solar meridian (north positive) and latitude circle (west positive) through disk center. The $(L_{\rm cen}, B_{\rm cen})$ coordinates specify the corresponding heliographic longitude and latitude of the field center midway the sequences. Figure 1 shows the field
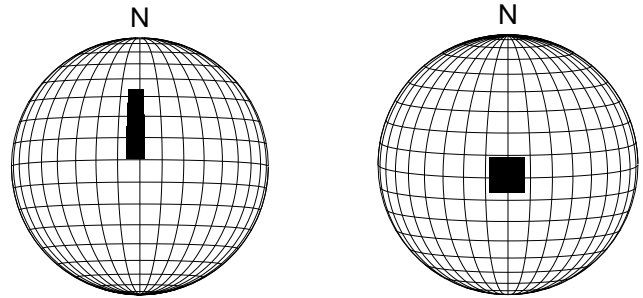
orientations. Figures 2 and 3 show sample 1700 Å images from the May 12 and October 14 sequences, respectively. The intensity scaling is logarithmic in order to accommodate both network and internetwork variations; this is the case for all greyscale image displays in this paper. The May 12 field contained some active network. The October 14 field sampled an area that was very quiet. Both fields where divided into smaller subfields to fit our computer memory during the analysis.

Solar rotation causes a drift of the entire field during the observation period while differential rotation causes differential drifts within the field. The split of the May 12 field into four subfields and of the October 14 field into two subfields, each covering 256 px in $Y$, reduces the differential variation. Each subfield was "derotated" by co-alignment through cross-correlation. This was done for the four May 12 subfield sequences by aligning each frame to the average of 10 mid-sequence frames. Direct comparison between different wavelengths was made possible by co-aligning each subfield sequence to the corresponding 1600 Å one.

The longer duration of the October 14 subfield sequences (nearly four hours) and the consequent evolution of the solar scene necessitated a more elaborate three-step alignment procedure. It consisted of first aligning each sequence of 20 images to the last previously aligned image, then replacing image shifts above three-sigma rms value by the average shift of the preceding and subsequent images in order to reduce pointing jitter extremes, and finally co-aligning all images per sequence to the 1600 Å sequence. The resulting October 14 alignments are generally accurate to a few tenths of a pixel. The May 12 alignments show larger displacements and were smoothed through $3 \times 3$ pixel spatial boxcar averaging.

These alignments make fixed-pixel locations $(X, Y)$ in each $(X, Y, t)$ sequence correspond to fixed solar locations with respect to the local co-rotating solar frame. The rotation produces incomplete solar sampling at the east and west field edges where pixels rotated in or out of the field during the sequence. These are excluded from the measurements below by using edge masks as illustrated in Fig. 4.
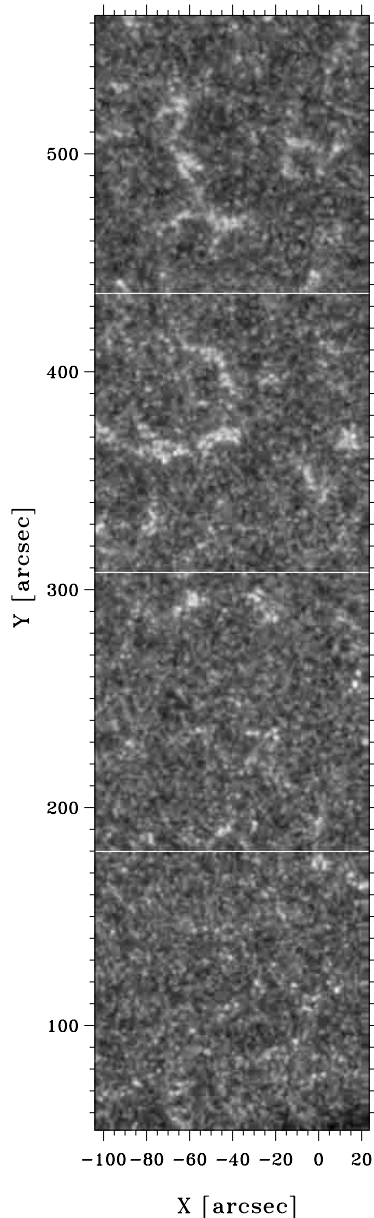
**Fig. 2.** Sample image taken by TRACE on May 12, 1998, at 15:26:32 UT in the 1700 Å passband. The upper half contains stronger network. Axes: solar $X$ and $Y$ in arcsec from disk center. The greyscale is logarithmic in order to bridge large contrast. The field was split into the four indicated subfields for this analysis.



**Fig. 3.** Sample image taken by TRACE on Oct. 14, 1998, at 10:05 UT in the 1700 Å passband. The observed area was very quiet. Axes: $X$ and $Y$ in arcsec from disk center, same scale (on the paper) as in Fig. 2. Greyscale: logarithmic. The field was split into two subfields as indicated. The horizontal striping at right marks incomplete sampling which results from solar rotation correction.

large brightness. Network/internetwork masks were constructed from the three successive 1600 Å histograms per subfield by assigning a pixel to be "internetwork" if its average brightness was below the Gaussian peak location in all three histograms, to be "network" if it belonged in all three histograms to the non-Gaussian high-intensity tail demarcated in Fig. 4, and to be "intermediate" if it fell between these extremes in all three histograms. Pixels that changed category between the three histograms were excluded. The mask that resulted for the May 12 top subfield is shown at lower right in Fig. 4. It restricts the pixels labeled network to the brightest areas in the first panel of Fig. 14 and the internetwork to rather small "heartland" regions relatively far from network, with a large zone of intermediate-category pixels (light grey) separating the two.

**Network/internetwork separation.** Each observed subfield was divided into network, internetwork, and remaining area called "intermediate". The latter may (and indeed does) mix properties of the two regimes and was introduced at appreciable fill factor in order to achieve better isolation of characteristic properties of the network and internetwork, respectively.

The separation was defined in terms of the average 1600 Å brightness per pixel over periods of 30 min for May 12, 80 min for October 14. The more stably present network patches survive such averaging, whereas the faster varying internetwork emission is washed out (compare the sequential variations in Fig. 5 with the 30-min average in the first panel of Fig. 4 and with the 90-min average in the first panel of Fig. 14). The upper-right panel of Fig. 4 shows a sample 30-min brightness distribution in the form of a histogram. It is characteristic for all our data and shows a Gaussian peak with an extended tail towards
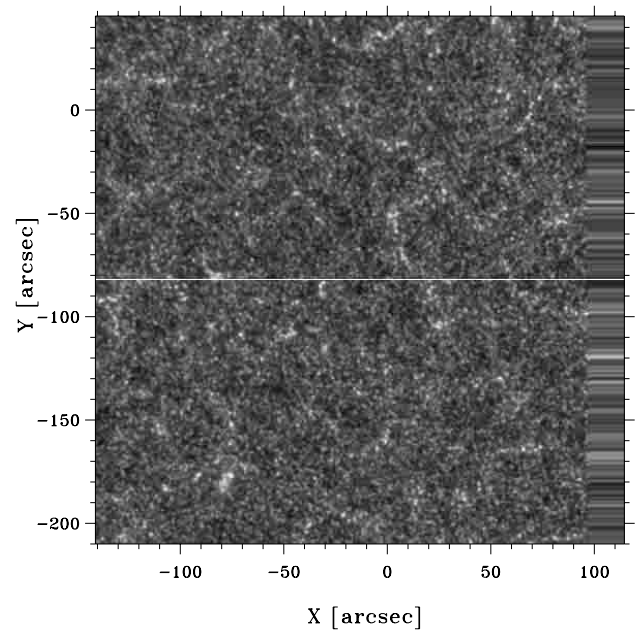
## 3. Fourier analysis

We briefly review our evaluations of Fourier quantities from the TRACE data. The analysis is standard following Edmonds & Webb (1972), Paper I, and Lites et al. (1998), but there are various display choices that require discussion. We write the temporal Fourier transform of a time sequence $f_1(x, y, t)$ for solar location $(x, y)$ as

$$F_1(x, y, f) = a_1(x, y, f) + i\, b_1(x, y, f) \qquad (1)$$

where $a_1$ and $b_1$ are real numbers, $t$ represents time and $f$ temporal frequency. The subscript 1 indicates a particular TRACE sequence. The cross-correlation spectrum
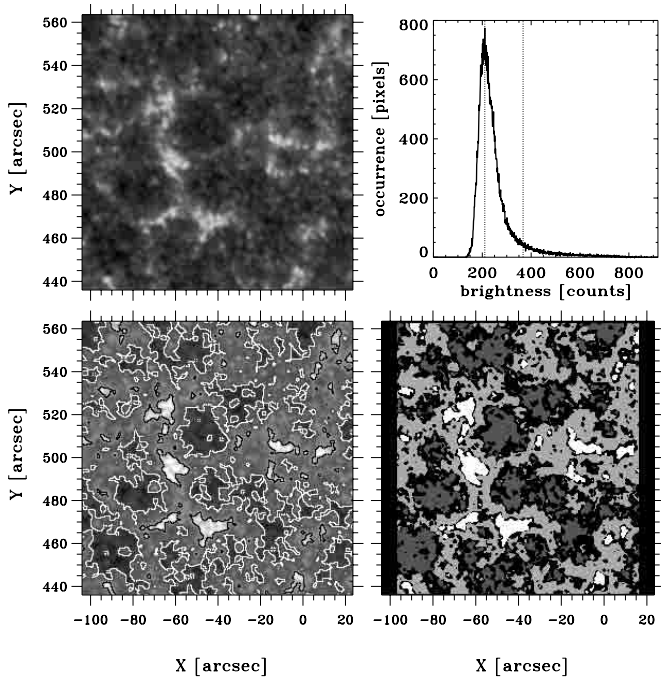
**Fig. 4.** Network and internetwork masks for the top subfield of the May 12 data shown in Fig. 2. Upper left: 30-min average (15:00–15:30 UT) for 1600 Å, logarithmic greyscale, $X$ and $Y$ axes in arcsec from disk center. Upper right: histogram of the number of pixels per brightness bin in this average. Dotted lines: division into internetwork (left), intermediate (middle strip), and network (right) categories. Lower left: logarithmic average overlaid with white and black contours corresponding to the demarcations. Lower right: final mask resulting from three successive 30-min averages. Dark grey: internetwork. White: network. Light grey: intermediate category in all three averages. Black: pixels which switch category between averages, discarded. The left and right edges are sampled incompletely due to solar rotation tracking and are also discarded.

between two simultaneous sequences 1 and 2 per location $(x, y)$ is

$$
\begin{aligned}
F_{12}(x, y, f) &= F_1(x, y, f)\, F_2^*(x, y, f) \\
&= c_{12}(x, y, f) + i\, d_{12}(x, y, f)
\end{aligned}
\tag{2}
$$

where the asterisk indicates the complex conjugate and $c_{12}$ and $d_{12}$ are real numbers.

**Power normalisation.** Standard choices for the display of power spectra are to plot the modulation energy

$$
P_E(x, y, f) = a(x, y, f)^2 + b(x, y, f)^2,
\tag{3}
$$

the fractional modulation

$$
P_f(x, y, f) = \frac{a(x, y, f)^2 + b(x, y, f)^2}{a(x, y, 0)^2 + b(x, y, 0)^2},
\tag{4}
$$

or to use Leahy normalisation

$$
P_{\mathrm{L}}(x, y, f) = \frac{a(x, y, f)^2 + b(x, y, f)^2}{\sqrt{a(x, y, 0)^2 + b(x, y, 0)^2}}
\tag{5}
$$

(Leahy et al. 1983, cf. van der Klis 1989, Appendix of Doyle et al. 1999). The latter serves to estimate the significance of periodic signals but is not used here.

This choice in normalisation does not affect the relative shape of an individual power spectrum but becomes important when comparing or averaging different signals. For example, if some wave process dissipates the same amount of energy at the wave frequency both in network and internetwork locations, using (3) without normalisation is appropriate. Fractional power normalisation (4) would underestimate the network dissipation in that case because network is consistently brighter, but it becomes the right measure when both network and internetwork are affected by the same multiplicative modulation process. We illustrate such differences below.

**Phase differences.** The phase-difference spectrum is

$$
\Delta\phi(x, y, f) = \arctan\left(\frac{d_{12}(x, y, f)}{c_{12}(x, y, f)}\right)
\tag{6}
$$

where positive values of $\Delta\phi$ imply that signal 1 is retarded with respect to signal 2. Different strategies exist to display and average phase differences $\Delta\phi$. The simplest one is to simply display all samples per temporal frequency in an unweighted scatter diagram (e.g., Gouttebroze et al. 1999), neglecting the amplitudes of the contributing Fourier components, or to display the scatter point density as brightness (e.g., Kneer & von Uexküll 1993). Another extreme is to display only spatial averages per frequency through averaging over a spatial wavenumber $k_h$ segment or an annulus in the $(k_x, k_y)$ spatial transform plane (e.g., Deubner et al. 1992). We prefer, as in older work, to visualise also the scatter itself in order to permit appreciation of its distribution. Lites & Chipman (1979) applied weighting per $(x, y, f)$ sample by the cross-power amplitude $\sqrt{P_1 P_2}$ (with $P_1 = a_1^2 + b_1^2$ and $P_2 = a_2^2 + b_2^2$) to produce binned greyscale $\Delta\phi$ displays with normalisation per temporal frequency bin. In Paper I only the samples with the highest mean Fourier amplitude $(\sqrt{P_1} + \sqrt{P_2})/2$ were plotted as scatter diagrams.

In this paper we show binned greyscale scatter plots with cross-power amplitude sample weighting following Lites & Chipman (1979).

We overlay spatially-averaged phase difference curves following Lites et al. (1998), given per sampled frequency by

$$
[\Delta\phi]_{xy}(f) = \arctan\left(\frac{[d_{12}(x, y, f)]_{xy}}{[c_{12}(x, y, f)]_{xy}}\right)
\tag{7}
$$

where the square brackets express averaging over locations $(x, y)$. This procedure equals vector addition of the individual cross-correlation samples with each vector length set by the product of the two Fourier amplitudes so that the cross-power amplitudes again act as weights in setting the slope of the summed vector. The procedure avoids wraparound errors that occur in straightforward averaging from the arctan evaluation, for example when a value
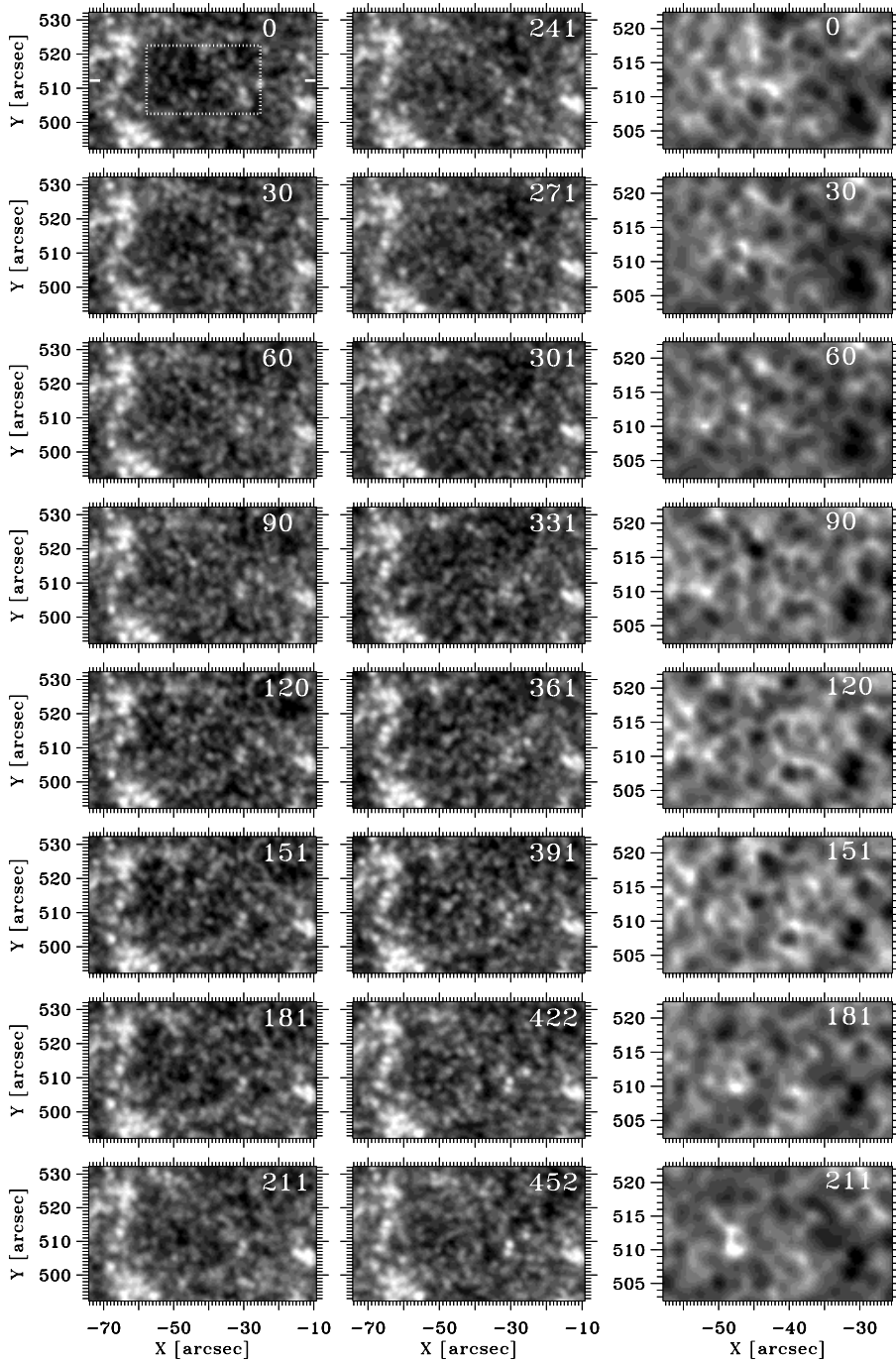
**Fig. 5.** Partial cutouts from the May 12 1700 Å sequence illustrating temporal variations at 30 s cadence. The numbers specify elapsed time from 15:26:32 UT in seconds. Axes: $X$ and $Y$ in arcsec from disk center. The greyscale is logarithmic. The first panel is a central cutout of the top panel in Fig. 2.

The white markers along the sides of this panel specify the horizontal cut location used in Figs. 6–7. The white box marks the yet smaller subfield which is duplicated in the third column using a sign-reversed logarithmic greyscale to display the slowly-varying internetwork background pattern. Taking the inverse emphasizes the internetwork features by darkening the network and makes the brightness minima of the three-minute oscillation appear as brightest features. These reversed extrema appear to travel fast along the strands of a more persistent background mesh which we attribute to gravity-wave interference. Similar behaviour is seen, in counterphase, for the bright internetwork grains on non-inverted but rapidly displayed movies such as the ones on URL http://www.astro.uu.nl/~rutten/trace1 from which this figure is derived. The grain-to-mesh superposition is also visualized in Fig. 11.

just above $\pi$ is transformed into one just above $-\pi$ and then averages erroneously with one just below $\pi$ to $\Delta\phi \approx 0$ instead of $\Delta\phi \approx \pi$.

Coherence. There is also a choice for the evaluation of the degree of coherence between two signals. It requires some sort of local temporal or spatial averaging, because without any smoothing the coherence between two sinusoidal Fourier components at given $(x, y, f)$ is unity regardless of the corresponding Fourier amplitudes and phase

difference. The Würzburg practice of annular $k_h$ averaging has the advantage that adjacent frequencies are treated independently, but the disadvantage that the modulations are assumed isotropic. Note that in this case the mean coherence goes to zero for pure noise. In contrast, Lites and coworkers treat each spatial pixel as an independent sample of solar behaviour but average over a frequency interval (Paper I[1], Lites et al. 1998), a tactic necessarily followed

[1] The angle brackets and squares in Eq. (4) of Paper I are in the wrong order (but not in the actual code used there).

also in the one-dimensional phase modelling of Skartlien et al. (1994). For pure noise this procedure yields positive coherence $C = 1/\sqrt{n}$ when averaging a sufficiently large sample, with $n$ the number of frequency resolution elements per averaging interval. We use the latter method, selecting boxcar frequency smoothing that is represented by angle brackets in writing the coherence as

$$C^2(x, y, f) \equiv \frac{< F_{12} >< F_{12}^* >}{< F_1^2 >< F_2^2 >} \qquad (8)$$

$$= \frac{< c_{12} >^2 + < d_{12} >^2}{< a_1^2 + b_1^2 >< a_2^2 + b_2^2 >}. \qquad (9)$$

The spatially averaged coherence per frequency is then:

$$[C^2]_{xy}(f) = \frac{[< c_{12} >^2]_{xy} + [< d_{12} >^2]_{xy}}{[< a_1^2 + b_1^2 >< a_2^2 + b_2^2 >]_{xy}}. \qquad (10)$$

Fourier reduction. We determined and Fourier-transformed the temporal brightness variation per pixel using equidistant time sampling with closest-neighbour image selection as discussed above, 10% cosine bell windowing, and replacing the zero-frequency transform values by the original mean brightness. We applied frequency smoothing for the coherence evaluations with $n = 5$ so that pure noise has $C = 0.45$. The phase differences between different TRACE passbands were corrected for the temporal shifts between their respective sampling scales. The shifts result from the sequential TRACE image taking and produce artificial phase shifts that increase linearly with frequency when measured as phase-difference angle. Other effects from the sequential sampling are discussed in Sect. 6.

The resulting Fourier power spectra, phase-difference spectra and coherence spectra per solar location were spatially averaged over the network and internetwork pixel categories, respectively. We do not show results for the intermediate pixel category when these are indeed intermediate between network and internetwork.

## 4. Results

### 4.1. Spatio-temporal behaviour

Sample images and timeslices. Figure 5 illustrates the dynamical nature of the solar atmosphere sampled by the 1700 Å passband in the form of a short sequence of small cutouts from the May 12 top subfield shown in Fig. 2. The cutout contains network at left and right, and internetwork in the center. The greyscale is logarithmic to show the grainy nature of both network and internetwork in these displays, which resemble Ca II K line-center filtergrams. Each of the network grains results probably from multiple close-lying magnetic elements in the photosphere (we tried but did not succeed to obtain simultaneous G-band imaging with the Swedish Vacuum Solar Telescope to resolve the chromospheric network into photospheric magnetic element clusters). The internetwork
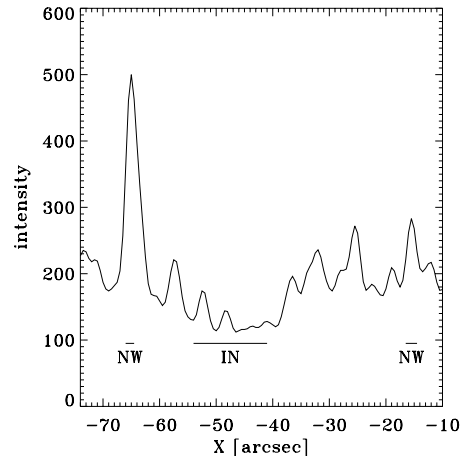


**Fig. 6.** Linear intensity variation along $Y = 512.5$ arcsec in the first panel of Fig. 5. The same cut location is used for the $X-t$ slices in Fig. 7. The short bars specify the small segments selected as network and internetwork by the mask in Fig. 4.

area contains bright grains that appear only briefly, for example at $x = -45$, $y = 516$ in the $\Delta t = 90$ panel. The network grains vary also with time, but are generally more stable.

The third column in Fig. 5 shows further enlargements of the cutouts in the first column with sign-reversed logarithmic greyscaling. The flip in contrast emphasises the spiderweb background pattern to which we return below.

Figure 6 shows actual linear intensity along the cut defined by markers in the first panel of Fig. 5. The high peak at $X = -65$ and the peak at $Y = -25$ are network grains; the others are internetwork grains with the one at $X = -33$ a "persistent flasher" (see below). The bright grains ride as enhancements on a general background, as shown already by Foing & Bonnet (1984a). The severity with which the mask defines network and internetwork is illustrated by the shortness of the corresponding cut segments, with only the darkest background classified as internetwork. The flasher is located in the generally brighter intermediate zone.

The traditional way of displaying spatio-temporal variability is to construct space-time plots or "timeslices". Figure 7 shows examples in the form of $X-t$ graphs that cover the full May 12 sequence temporally but only the $Y = 512.5$ cut marked in the first panel of Fig. 5 spatially. The sequence in Fig. 5 samples only the brief duration between the white markers in Fig. 7. The $X-t$ slices in Fig. 7 resemble spectrometer data taken with the slit programmed to follow solar rotation (the format is directly comparable to many time evolution displays in the SUMER papers listed in the introduction). They typically show network as bright striping and internetwork oscillations (when present) as dappled grain sequences at lower brightness. Square-root or logarithmic greyscaling or subtraction of the mean intensity per pixel is usually required to enhance the visibility of the internetwork brightness modulation. Figure 7 illustrates this morphology with a
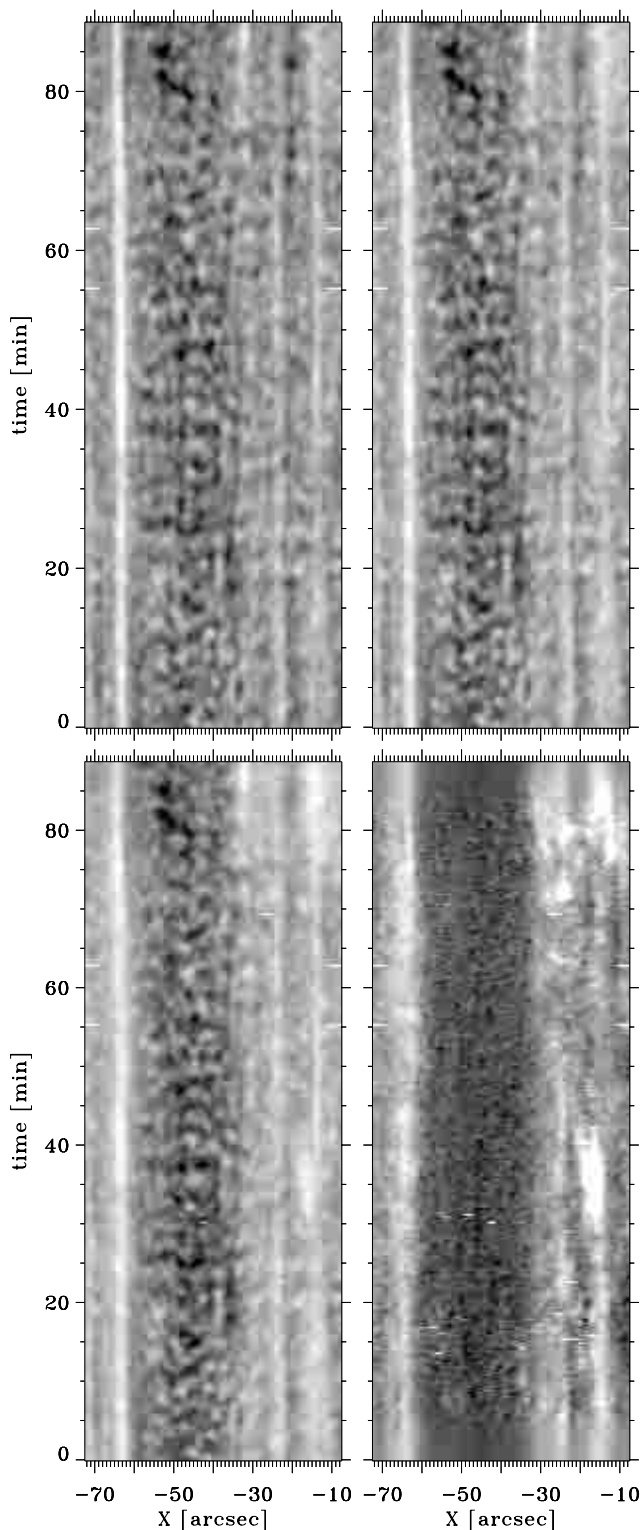
**Fig. 7.** Partial $X-t$ slices from the May 12 sequence at $Y = 512.5$ arcsec, illustrating temporal behaviour of network patches (bright stripes) and internetwork oscillations (grains on dark background). Axes: $X$ in arcsec from disk center, elapsed time in minutes covering the full sequence duration. Panels: upper left 1700 Å, upper right 1600 Å, lower left 1550 Å, lower right C IV construct. The snapshots in Fig. 5 sample the 7.5 min period between the white markers. Greyscale: logarithmic, clipped for C IV. Bright horizontal dashes result from cosmic ray hits.

bright network grain at left, some weaker network grains at right, and internetwork oscillations in the dark area around $X = -50$. The oscillatory internetwork patterning is roughly equal in the three TRACE passbands, but the network features become brighter and coarser at shorter wavelength. Additional emission contributed by the C IV lines shows up in the 1550 Å panel and dominates in the C IV construct. The internetwork parts of the latter are very noisy.

A general comment with respect to Figs. 5 and 7 is that such cutouts and slices constitute a poor proxy for viewing the data cubes in fast on-screen computer display. We use an IDL "cube slicer" developed by C.A. Balke to view concurrent $(X, Y, t_0)$, $(X, Y_0, t)$ and $(X_0, Y, t)$ plane cuts through multiple data cubes simultaneously, with mouse control to select and move the $X_0$, $Y_0$ and $t_0$ cut location with co-moving cross-hairs in each, up to nine co-changing movie and timeslice panels in total. It enables inspection of such data sets using visual pattern recognition of variations, correlations, time-delay relationships, etc. Such slicing through TRACE data cubes makes one appreciate fully the richness and the variety of the solar scene – effectively sampling a manifold instead of the single cut plotted in a timeslice or observed by a spectrograph slit, and with displacements of one arcsec already showing significant pattern difference. The next-best option is to play TRACE sequences as movies, for example with SolarSoft Xstepper (URL `http://www.lmsal.com/solarsoft/`) or the ANA browser (URL `http://ana.lmsal.com/`). We urge the reader to do so in order to appreciate the dynamical nature of the quiet-Sun internetwork, and have made sample TRACE movies from this work available at URL `http://www.astro.uu.nl/~rutten/trace1`.

What do we see in our TRACE datacube visualizations? Just as on Ca II $K_{2V}$ movies from ground-based telescopes, the network grains appear as islands of stability in an internetwork sea made up of fast-changing grainy emission features that are superposed on a spiderweb background mesh which is modulated with three-minute periodicity but evolves much slower. The internetwork background is best seen in negative, as in the third column of Fig. 5, because its mesh structure then stands out without visual contamination from the brighter network and internetwork grains. It then resembles reversed granulation with 2–5 arcsec cell size, but it cannot be just that since it shows large three-minute modulation. It was detected by Martić & Damé (1989) as a 8 Mm spatial power peak in a 4.5 min sequence of TRC 1560 Å filtergrams that was Fourier-filtered passing three-minute modulations; the reverse display in Fig. 5 shows it directly without Fourier tuning. The pattern becomes fuzzier with height: the 1700 Å sequences show it sharper than the 1550 Å sequences.

The internetwork grains appear as localised enhancements of the background mesh pattern. They are not as sharp and bright as on $K_{2V}$ filtergrams but show similar rapid morphology changes on a 2–4 min time basis. Sometimes, they reappear a few times at locations
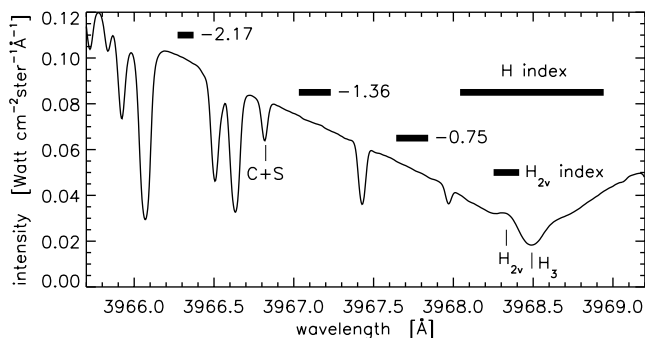
**Fig. 8.** Ca II H segment of the disk-center spectrum atlas of Neckel (1999). The horizontal bars mark spectral windows used in Paper I for oscillation measurements shown below. The label C+S identifies the Fe I line used by CS1997 to derive subsurface piston driving in their numerical simulation of the Ca II H line core behaviour in the same data.

within soundspeed (7 km s$^{-1}$) travel distance. Fairly frequently, pairs of grains 5–10 arcsec apart brighten repeatedly in phase. Other grains appear only once. Many brightenings move with apparent supersonic speeds, up to 100 km s$^{-1}$, along the strands of the background mesh pattern. Such travel is more obvious for the darkest locations seen as bright in reversed-greyscale display, peaking when such traveling enhancements "collide" at mesh strand junctions. Occasionally, the timeslices exhibit wavy patterns that indicate oscillatory coherence over spatial scales as long as 20 arcsec. The reversed-greyscale movies also display slower modulation in which the mesh junctions brighten (darken in reality) together in patches covering about 10–20 arcsec. Such large-area coherence was noted already by Cook et al. (1983).

**Comparison with Ca II H & K.** It is of interest to compare the TRACE ultraviolet timeslices in Fig. 7 with Ca II H & K results using similar display formats. Most Ca II K filtergram movies are made with passbands between 0.5 and 3 Å, integrating over a fairly wide segment of the Ca II K core and mixing K$_3$ line-center variations with the K$_{2V}$ grain and inner-wing whisker phenomena (cf. Rutten & Uitenbroek 1991a). This implies both a wider response function including contributions from lower heights as well as phase averaging for upwards propagating waves. The difference in signature can be displayed from spectrogram sequences by integrating over appropriate spectral passbands. Such a comparison is shown between the Ca II H$_{2V}$ feature and the passband of the Mount Wilson H & K photometer in Fig. 2 of Rutten (1994) and Fig. 1 of Rutten et al. (1999a), based on the Ca II H spectrum sequence of Lites et al. (1994) taken in 1991 at the NSO/Sacramento Peak Dunn Solar Telescope. It shows that limiting the bandpass to the K$_{2V}$ feature itself produces sharper grains with higher contrast than from the integrated Ca II H core, but also that the dynamical time-slice patterning is quite similar for the wider passband.
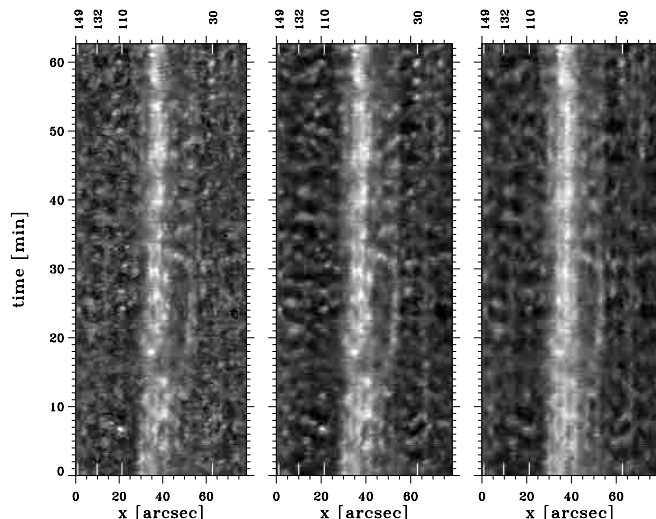


**Fig. 9.** Ca II H $X-t$ slices from the data analysed also in Paper I. Left: Ca II H$_{2V}$ peak brightness. Middle: Ca II H$_{2V}$ index = brightness integrated over $3968.33 \pm 0.08$ Å. Right: Ca II H index = brightness integrated over $3968.49 \pm 0.45$ Å. Bright column markers: solar locations simulated by CS1997, with the "slit positions" specified by them added at the top. A Fourier decomposition of the middle slice is shown in Fig. 10.

We add a similar timeslice comparison in Fig. 9 that is based on the Ca II H spectrum sequence of Paper I taken with the Dunn telescope in 1984. These data have special interest for internetwork dynamics because they were numerically simulated in great detail by CS1997. Figure 8 identifies various spectral features discussed here and below. The first panel of Fig. 9 measures the peak brightness of the Ca II H$_{2V}$ emission feature (following its wavelength shifts), the middle panel integrates brightness over a stable 0.16 Å band around its mean location (H$_{2V}$ index), and the rightmost panel integrates brightness over a 0.9 Å wide band around mean line center. The noise decreases with bandpass width. The second panel gains grain contrast by sampling low intensity when the H$_3$ core shifts into the H$_{2V}$ passband. The third panel shows the internetwork grains at lower contrast and appreciably fuzzier due to response smearing, but nevertheless, the dynamical morphology is similar in all three panels. Thus, wider-band Ca II K movies are indeed suited to study the spatio-temporal patterns of the oscillations that cause K$_{2V}$ and H$_{2V}$ grains.

CS1997 simulated the four solar locations that are marked in Fig. 9 and are labeled with the slit positions specified in their paper. Their simulations reproduced the spectral grain occurrence patterns at positions 110 and 132 remarkably well (their Plate 20). They computed too many and overly bright grains for positions 149 and 30 – which they attributed to a preceding computational excess of high-frequency (14 mHz) oscillations – but nevertheless, the overall agreement between the simulated and observed Ca II H spectral behaviour is impressively good. This success has brought general acceptance of the notion that K$_{2V}$ internetwork grains are primarily an acoustic

weak-shock phenomenon as advocated by Rutten & Uitenbroek (1991a, 1991b).

The ultraviolet slices in Fig. 7 are very similar to the wider-band Ca II H slice in the rightmost panel of Fig. 9. The TRACE images therefore appear to have adequate angular resolution to display grain patterns similarly to a 1 Å Ca II K filtergram sequence. The considerable spectral width of the TRACE passbands must cause considerable height-of-formation and propagative phase mixing, so that the 1 arcsec TRACE resolution is perhaps not too far from the intrinsic detail observable in these passbands. The direct comparison of a selected Ca II K image with simultaneous TRACE images in Fig. 2 of Rutten et al. (1999a) demonstrates that TRACE is not resolving the grains as well as a 3 Å Ca II K filter at excellent La Palma seeing. Note that the ultraviolet continua sampled by TRACE are affected by bound-free scattering which is similar to the bound-bound resonance scattering affecting Ca II K (cf. Fig. 36 of Vernazza et al. 1981; Figs. 2–4 of Carlsson & Stein 1994; lecture notes by Rutten 2000) and produces similar smearing of the source function response to thermal fine structure along the line of sight.

Apart from its lower resolution the 1700 Å image in Fig. 2 of Rutten et al. (1999a) is virtually identical to the Ca II K image. The Ca II slices in Fig. 9 show several episodes of reduced seeing quality (greyish horizontal wash-outs) that do not occur in the TRACE slices. Thus, the TRACE ultraviolet passbands sample network and internetwork much as 1–3 Å Ca II K passbands do – but they do so seeing-free, without geometrical distortions or temporary degradations.

Internetwork background. The grains represent the most striking feature in the internetwork parts of Ca II K and ultraviolet filtergram sequences, but there is also the spiderweb emission pattern that makes up the greyish background in Figs. 5–7. It is observed most clearly in reversed-greyscale movies as the one at URL http://www.astro.uu.nl/~rutten/trace1, here emulated by the third column in Fig. 5, has 2–5 arcsec mesh size, is modulated with 2–4 min periodicity, and evolves at longer time scales. Enhancements (both brightenings and darkenings, the latter standing out more clearly in reversed-greyscale display) travel at large apparent speed along the strands (cf. Fig. 3 of Lites et al. 1999). Internetwork grains occur always as local, point-like enhancements of the mesh in its bright phase, as emphasised by Cram & Damé (1983) whose $V/R$ timeslice shows the background as a "wavy curtain" oscillatory pattern with considerable spatial extent (cf. Rutten & Uitenbroek 1991a).

Figure 10 analyses the internetwork background and grain occurrence with another unpublished display from the 1984 Ca II H data of Paper I. The upper part is a Fourier decomposition of the $H_{2V}$ index slice in Fig. 9 into low-frequency, five-minute and three-minute oscillatory components, similar to the $H_{2V}$ decompositions of
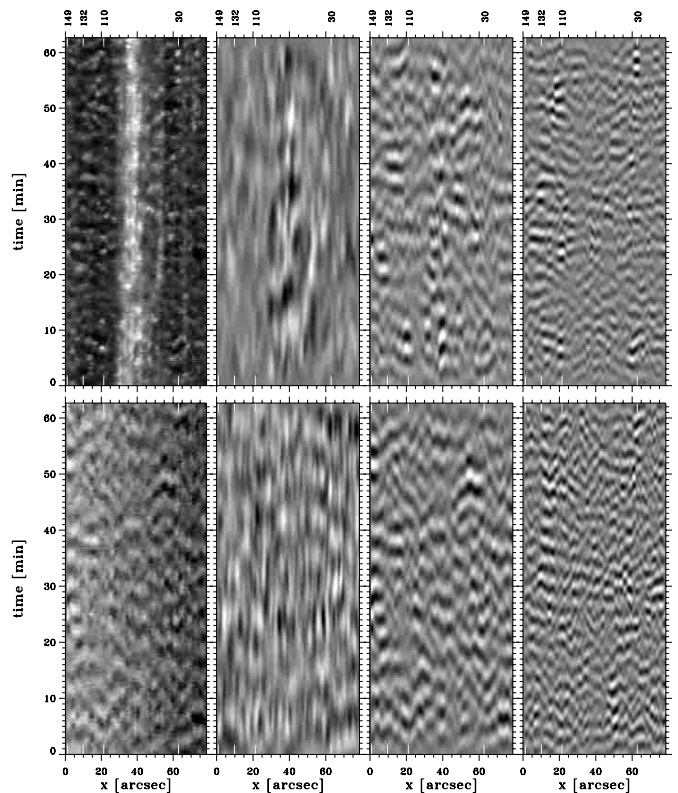


**Fig. 10.** Fourier-decomposed timeslices of the spectral data presented in Paper I. Upper panels: Ca II $H_{2V}$ decomposition. The $H_{2V}$ brightness slice at left is also shown in Fig. 9. The other panels display its decomposition into low-frequency modulation, five-minute modulation and three-minute modulation, obtained by temporal filtering of the sequence for each spatial position along the slit. The greyscale is set to maximum contrast for each panel independently. Lower panels: similar decomposition for the Dopplershift of Fe I 3966.82 Å, the blend from which CS1997 derived a subsurface piston to simulate the intensity in the upper panels at the locations marked along the top.

1991 data in Fig. 4 of Rutten (1994) and Fig. 6 of Rutten (1995). The split is obtained by temporal Fourier filtering per spatial $x$-position along the slit, so that adjacent columns are independently decomposed. As in any timeslice, horizontal structures imply instantaneous spatial coherence in the spatial direction while tilted structures suggest motion along the slit (real motion for a round feature, but for an elongated one moving at a small angle the apparent velocity of the slit-feature intersection exceeds the real motion). The lower part of Fig. 10 decomposes the simultaneously measured Dopplershifts of the photospheric Fe I line from which CS1997 obtained their subsurface piston excursions. The Fe I low-frequency panel (second in bottom row) presumably shows granular overshoot and/or internal gravity waves. The Fe I five-minute and three-minute panels show wavy-curtain patterns with considerable propagative spatial coherence and finer substructure at shorter periodicity. They extend across the network strip without obvious pattern change. The chromosphere (upper panels) shows qualitatively similar patterns, with

appreciable correspondence with the underlying photospheric pattern at least for the five-minute components in internetwork areas. The $H_{2V}$ low-frequency panel (second in upper row) is the only modulation panel in which the presence of network (strip at $x = 30-40$ arcsec) is recognisable, having slower and larger-amplitude modulation than the internetwork areas on both sides.

The photospheric wavy-curtain patterns in the third and fourth lower panels represent interference between the ubiquitous acoustic waves of the global and local $p$-mode oscillations that dominate the dynamics of the middle photosphere where convective motions have died out. The similar patterns in the upper row indicate that the rapidly varying modulation of the internetwork background mesh in Ca II K and ultraviolet filtergram movies is also dominated by acoustic wave interference. However, the background pattern in the low-frequency panels differs morphologically between the upper and lower rows, without obvious direct correspondence.

The internetwork grains in the first panel occur at spatio-temporal locations where the decomposed brightnesses to the right sum up to a bright total. For example, the bright grain at $t = 7$ min in Carlsson-Stein column 110 marks coincidence of bright five-minute and bright three-minute phases as present in a broad-band impulse. A much weaker grain follows after five minutes because the three-minute modulation is then out of phase. A sequence of bright grains at three-minute periodicity, as the one at the top of Carlsson-Stein Col. 30, requires the combination of strong three-minute modulation, weak five-minute modulation, and a bright phase of the low-frequency modulation in the second panel. The component weighting follows the $H_{2V}$ power spectrum which is similar to the $H_{2V}$ index power spectra shown in Fig. 21 and is dominated by the three-minute modulation.

The chromospheric background pattern, its three-minute modulation, and the internetwork grain superposition on this pattern become more evident in timeslices when these are severely compressed in the time direction and clipped as in Fig. 11. The internetwork background pattern shows up as dark and bright structures of 20–40 min duration with three-minute modulations that often seem spatially coherent over lengths of 5–10 arcsec, occasionally as long as 20 arcsec – much longer than the coherence extents evident in Figs. 7 and 9–10. This is because the compression reduces the tilts caused by the apparent motion of brightenings and darkenings along the strands of the background pattern, so that the eye interprets the total travel distance as a single coherent feature. A similar pattern seen in Dopplershifts of C II and O VI lines from SUMER was reported by Wikstøl et al. (2000) as a new phenomenon with unexpectedly large spatial coherence, but their timeslice is similarly compressed.

Persistent flashers. Some internetwork grains seem to mark a location with longer spatial memory than 5–10 min by reappearing repeatedly, sometimes with extended
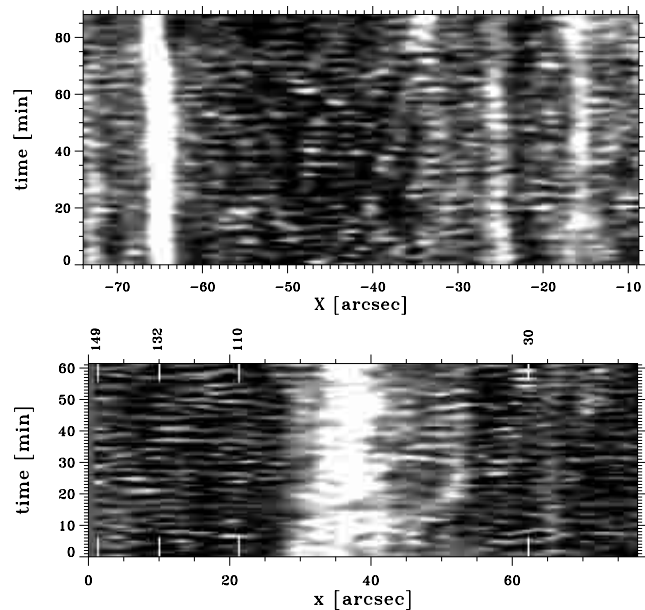


**Fig. 11.** Compressed timeslices. Upper panel: the 1700 Å data of Fig. 7 compressed in the time direction, expanded in the spatial direction, and clipped in greyscale so that the network becomes heavily saturated. Lower panel: similar format for the Ca II $H_{2V}$ index data in the middle panel of Fig. 9, including Carlsson-Stein markers. The internetwork background mesh shows up as 2–5 arcsec wide columns on which the three-minute oscillation is superimposed.

intervals of absence. An example is seen near $X = -33$ in the upper half of Fig. 7. A bright grain appears in the 1700 Å passband at $t = 62$ (also in the $\Delta t = 391$ panel of Fig. 5), seems to reappear at $t = 66$ and $t = 72$, and then to become part of a bright streak towards the end of the sequence. In the 1550 Å panel this location has enhanced brightness all the time (at least on our screen). What looks like an isolated 1700 Å grain at first sight is actually part of a long-lived (though modulated) brightness feature.

A particular $K_{2V}$ grain of this type has been described by Brandt et al. (1992, 1994), who found it by playing a video movie of Ca II K images very fast. It was occasionally absent for some time; fast movie display made its longer persistence recognisable. It flashed at 3–5 min periodicity when seen and it behaved as an actual solar "cork", the chromospheric emission patch following the surface flows derived from local correlation tracking of granulation features and migrating from cell center to network within a few hours.

Such intermittently present persistent features are not easily identified without movie display. Only when stationary in $Y$ do they become discernible in an $X-t$ slice by leaving an extended trail. We find that many isolated bright features which, when seen on a single frame might be taken to represent acoustic shock grains, are in fact such flashers, reappearing over a longer period and often with slightly higher background emission producing a thin trail between flashes in 1550 Å timeslices if the feature

doesn't move "off the slit". A shift of the slice position over one pixel (0.5 arcsec) often shortens or lengthens the apparent trail considerably. The sample slices in Fig. 7 contain a number of such weak long-duration streaks at right. The weakest ones fall in the intermediate pixel category in our mask definition and are not easily identifiable as network in Fig. 5. Only the dark area with dappled grain appearance around $X = -50$ in Fig. 7 seems to represent streak-less internetwork.

This split confirms the present conclusion from a long debate on magnetic internetwork grain anchoring (cf. Lites et al. 1999; Worden et al. 1999) that the internetwork areas may be locally dominated by grain-producing shock acoustics but may also contain features with a longer location memory that presumably mark magnetic field entities of sufficient strength to maintain an identity. We designate the latter "persistent flashers" following Brandt et al. (1992, 1994). The three features marked in Fig. 2 of Lites et al. (1999) represent other examples in the form of isolated chromospheric Ca II K grains that are clearly connected to photospheric G-band bright points of the type commonly believed to represent strong-field fluxtubes.

The flashers seem to appear more frequently near regular network. It is tempting to wonder whether such loose features build up the network or originate from it. The Brandt et al. flasher migrated from cell center towards network as one might expect for a split-apart ephemeral region marking field emergence. Our TRACE movies also show such cell-crossing flashers (plus some brightness features which move very fast along chromospheric mottles or higher-lying loops and stand out as such in the C IV-construct movie, see below), but most flashers appear fairly stationary near network and produce intermittent streaks lasting from half an hour to multiple hours with drifts below 10 arcsec. These may portray products of network shredding rather than network assembly.

By having a large intermediate pixel category we have eliminated most of the persistent non-network features from what our masks define as internetwork, a very stringent selection that should limit the internetwork Fourier results below to the darkest streakless regions in our data, such as the one around $X = -50$ in Fig. 7. Presumably, their brightness modulation is acoustically dominated.

## 4.2. Spatial modulation variations

Mask-averaged modulation. Figure 12 shows spatially averaged power spectra per mask category for the three ultraviolet wavelengths and the C IV construct. Fourier amplitudes ($\sqrt{P}$) are plotted on linear scales that are scaled per panel (wavelength) to the internetwork value at $f = 3$ mHz. This represents amplitude scaling analogous to Eq. (3). The heights of the different-category curves in each panel are directly comparable. Between panels, they are quantitatively comparable if the evanescent five-minute waves have similar brightness power at different heights in internetwork areas.

The curves in Fig. 12 show standard modulation behaviour (but with unprecedented precision) of network and internetwork. The brightness modulation power is highest at the lowest frequencies and reaches secondary maxima in the acoustic oscillation band, which grow in relative importance and in high-frequency extent with sampling height. Note that the acoustic peaks are less pronounced in these brightness modulation spectra
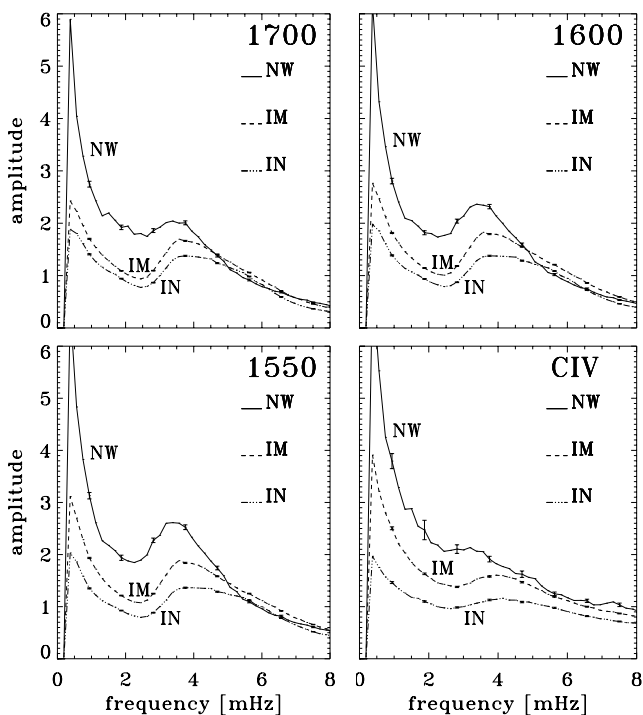


**Fig. 12.** Mask-averaged brightness modulation spectra from the May 12 sequences, split between the network (NW), intermediate (IM), and internetwork (IN) pixel categories. Each curve shows linear Fourier amplitude scaled by the internetwork value for that wavelength at $f = 3$ mHz, against temporal frequency. The mean value and trend (zero and first frequencies) are removed. Error bars: standard error of the average. Upper panels: 1700 and 1600 Å. Lower panels: 1550 Å and the C IV construct.
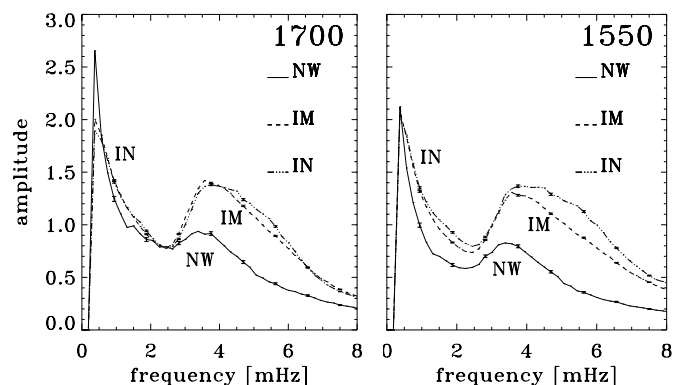


**Fig. 13.** Mask-averaged 1700 and 1550 Å fractional brightness modulation spectra, as in Fig. 12 but normalised by the temporal mean (zero frequency value, subtracted) per curve.

than they appear in Dopplershift samples from the same atmospheric domain, largely because Dopplershift modulation lacks prominent low-frequency modulation peaks. The acoustic peak is less clearly defined for the C IV construct.

Network power exceeds internetwork power up to $f = 5$ mHz but drops faster at higher frequencies. Higher up in the atmosphere, this distinction grows into fully disparate network-internetwork modulation behaviour, as illustrated below in Fig. 21. Around $f = 6$ mHz the intermediate-pixel category is no longer intermediate between network and internetwork but has the largest amplitude. We return below to these "power aureoles".

Choice of normalisation. Figure 13 duplicates the 1700 and 1550 Å amplitude spectra in the first column of Fig. 12, but after normalisation by the mean amplitude, showing fractional modulation analogous to Eq. (4). The amplitude scales again have unity at the 3 mHz internetwork value. In the lefthand panel the fractional modulation of network and internetwork appears roughly equal over $f = 0.5-3$ mHz. In the righthand panel the network category is lower than internetwork at all frequencies and the intermediate pixel class shows a "power shadow" for $f > 4$ mHz.

Comparison with Fig. 12 shows that the choice of normalisation affects the network/internetwork modulation ratio. It is not obvious which choice is physically preferable. The internetwork 3–6 mHz peak consists of acoustic waves (a mixture of the "photospheric five-minute" and "chromospheric three-minute" oscillations, where none of these names should be taken literally as meaning exclusive). The internetwork low-frequency peak is attributed to internal gravity waves (cf. Sect. 4.4). For these wave phenomena absolute power or amplitude specifies the importance of the wave itself, whereas fractional modulation scales the amplitude to the total time-averaged amount of photon emission which may be dominated by other processes. Even if the wave field inside network elements is the same as outside (fractionally or absolutely), the observed modulation does not need to be the same with either normalisation since density differences also affect the sampling height.

Spatially-resolved modulation. Figure 14 resolves the results in Fig. 12 spatially by displaying the brightness modulation per pixel for selected temporal frequency bands, with brighter greyscale indicating larger Fourier amplitude. Cuts along $Y = 500$ are shown in the top panels and display linear modulation amplitudes normalised by the mean of the whole subfield.

The first column represents the sequence-averaged intensities (zero-frequency modulation). The averaging increases the contrast between the fairly stable network and the rapidly varying internetwork. The logarithmic greyscale permits identification of the darkest internetwork areas; they correspond closely to the internetwork

pixel category (dark grey) of the mask in Fig. 4. The network grains appear coarser at shorter wavelength in these averages; the C IV construct looses detail. The network contrast increases towards shorter wavelength (cuts on top).

The second and third columns show modulation maps for slow variations, respectively with periodicities $P > 13$ min and $P \approx 5$ min. The network appears bright in the greyscale maps, with comparable modulation amplitudes at the different wavelengths (tracings at the top). Both the network and the internetwork areas are finely grained on a 1–2 arcsec scale in these long-duration modulation maps. There is no obvious morphology difference between high and small amplitude regions as in the short-duration modulation amplitude maps of Hoekzema et al. (1998b), probably due to pattern migration during the much longer durations that are Fourier-mapped here.

The normalised modulation amplitudes decrease with frequency (tracings at the top). At all three ultraviolet wavelengths the internetwork modulation gains amplitude with respect to the network modulation and exceeds the latter for frequencies $f \approx 4$ mHz. The rightmost column illustrates this in the form of dark patches that roughly correspond to the bright network areas in the first column. The high-frequency panel for the C IV construct (bottom right) does not show internetwork contrast reversal, but its internetwork areas are unreliable since these do not contribute C IV signal. The C IV construct images contain many artifacts from cosmic ray hits that have been removed.

Magnetic canopies. The C IV low-frequency amplitude map (second from left in the bottom row) differs strikingly from the other amplitude maps. It resembles a H$\alpha$ filtergram by showing the onset of fibrils extending away from the network. There is also a long curved arch in the upper-right corner. When viewing this C IV subfield as a movie, bright blobs are seen to be traveling along the arch at apparent speeds of about 100 km s$^{-1}$. The map also shows bright modulation patches that are much more pronounced than in the longer-wavelength panels, for example around $(-40, 530)$. These non-photospheric features indicate substantial contribution by the C IV lines that appears to be visualised easiest through their slow modulation. The fibril-like extensions are barely visible in the C IV $P \approx 5$ min map.

The C IV fibrils clearly depict magnetic field topology in which the field lines fan out from the network in the form of low-lying bundles. Magnetic canopies are a standard feature of magnetostatic fluxtube modelling (e.g., Spruit 1976; Solanki & Brigljevic 1992; Solanki & Steiner 1990) and were first reported by Giovanelli (1980) and Giovanelli & Jones (1982, 1983) who concluded that the fibrils observed in chromospheric lines such as H$\alpha$ map the actual canopies only partially, showing only those low-lying magnetic loops that have sufficient population density in the H I $n = 2$ level. We take the bright areas in the
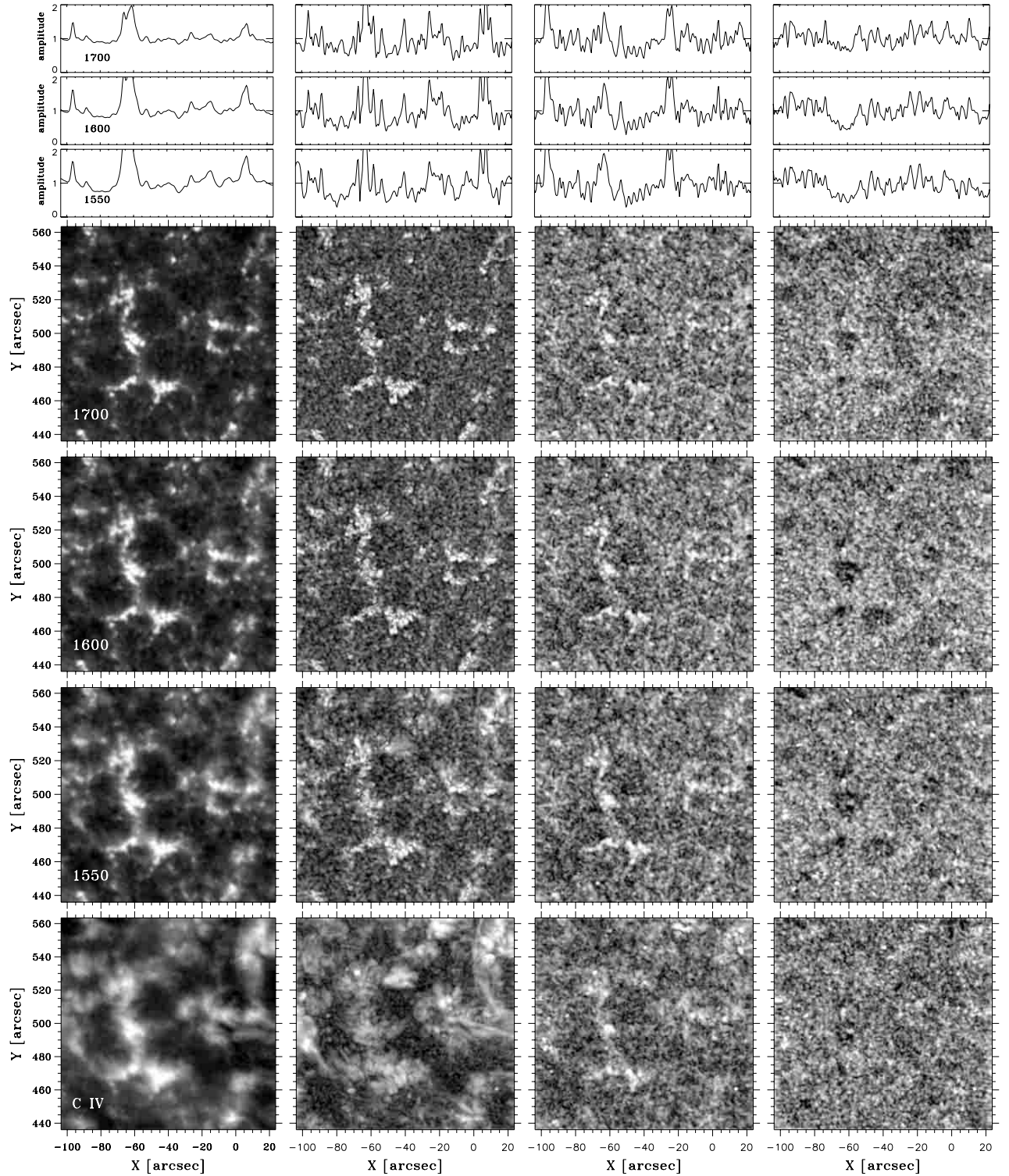
**Fig. 14.** Fourier modulation over the top subfield of the May 12 data. Axes: solar $X$ and $Y$ at mid-observation in arcsec. Greyscale: logarithm of the temporal Fourier amplitude ($\sqrt{P}$) of the brightness per pixel, clipped and rescaled per panel to improve display contrast. Columns from left to right: average intensity over the full 14:30–16:00 UT sequence duration (also with clipped logarithmic greyscale), Fourier amplitude in the 0.1–1.2 mHz frequency bin, in the 2.6–3.6 mHz bin (periodicity $P \approx 5$ min) and in the 6–8 mHz bin ($P \approx 2.5$ min). Graph rows: brightness modulation amplitude along $Y = 500$ for the 1700, 1600, and 1550 Å passbands, in linear units normalised by the mean modulation over the subfield. Image rows: brightness modulation maps for the 1700, 1600, and 1550 Å passbands and the C IV construct.

low-frequency C IV panel of Fig. 14 therefore as an incomplete indicator of canopy presence. The darkest areas in this panel correspond closely to the internetwork part of the mask in Fig. 4. This implies that the intermediate pixel

category that we derived from the mean 1600 Å brightness behaviour does not only correspond to more frequent occurrence of persistent flashers as discussed above, but also corresponds to the presence of overlying canopy fields that stretch out from the network over the adjacent internetwork at relatively low height.

Network aureoles. The amplitude spectra in Fig. 12 around $f = 6$ mHz and the rightmost column in Fig. 14 indicates the presence of weak "halos" or "aureoles" of enhanced high-frequency power around the network patches. They are seen as extended, though very patchy, bright rings around the dark areas marking network power deficits. They roughly cover the intermediate pixel zones and make the corresponding IM curves in the 1600 Å and 1550 Å panels of Fig. 12 exceed the other curves around $f = 6$ mHz.

Power aureoles at 3–min periodicity around plage were first reported from a chromospheric Ca II K image sequence by Braun et al. (1992) and from photospheric Dopplershift modulation maps by Brown et al. (1992) as patchy areas that contain small-scale 3–min modulation enhancements and are associated, but not cospatial, with magnetic regions. They were also seen in Ca II K image sequences by Toner & LaBonte (1991), in MDI Dopplergram sequences by Hindman & Brown (1998), and in local-helioseismic images constructed from MDI Dopplershift data by Braun & Lindsey (1999) who renamed them "acoustic glories" and suggested that the aureoles result from subsurface oscillation deficits underneath active regions as a result of wave refraction or scattering. Thomas & Stanchfield (2000) studied them in both the photosphere using a Doppler-sensitive iron line and the chromosphere using Ca II K, finding that the photospheric aureoles favour pixels of intermediate field strength but are not clearly related to the Ca II K aureoles. Hindman & Brown (1998) did not find aureoles in photospheric continuum intensity fluctuations in MDI data and use that to advocate that the halo oscillations are incompressible, a suggestion extended by Thomas & Stanchfield (2000) to the height of formation of their Fe I line.

The network patches in our quiet fields of observation represent much smaller field concentrations than the active regions in the aureole literature above and our TRACE data do not sample Dopplershift, which displays 3–min modulation much clearer than brightness at chromospheric heights (e.g., Cram 1978), but nevertheless the TRACE images bring additional information because they sample intrinsic brightness modulation in the upper photosphere that result from temperature and/or opacity variations without crosstalk from Dopplershifts.

Figures 15, 16 attempt to quantify the visual impression of aureoles in Fig. 14 by plotting 1600 Å Fourier power as a function of the distance of a pixel to the nearest network area with spatial averaging over the whole May 12 data set. Figure 15 is a frequency-resolved greyscale plot of this mean dependence for all pixels outside network.
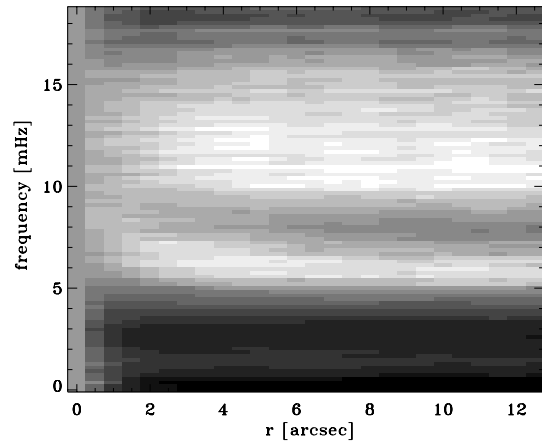


**Fig. 15.** Frequency-resolved aureole map, showing temporal power (grey scale) for the May 12 1600 Å data as a function of distance $r$ to the nearest network border, averaged over all non-network pixels in the whole May 12 field excluding edge pixels and normalised to the mean network power (value at $r = 0$, grey) per frequency bin.
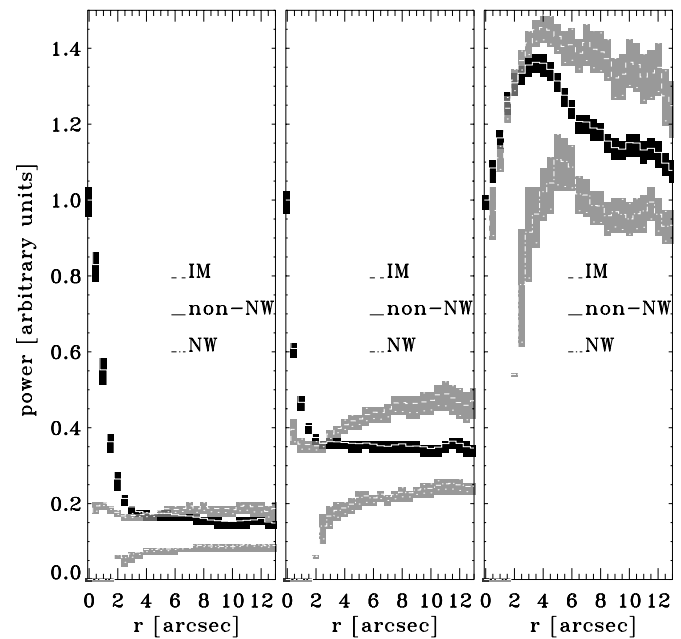


**Fig. 16.** Spatially-averaged modulation aureoles for different pixel categories. Each curve measures the mean temporal modulation power of the May 12 1600 Å data as a function of distance $r$ to the nearest network border, excluding edge pixels and normalised to the mean network power (the value at $r = 0$) per frequency bin. The shaded contours specify $3\sigma$ error estimates for each mean. Curves with dark contours: averaged over all non-network pixels in the whole May 12 field. Lower curves with grey contours: averaged only over all internetwork pixels. Upper curves with grey contours: averaged only over all intermediate-category pixels (light grey in Fig. 4). Panels from left to right: 0.1–1.2 mHz frequency bin, 2.6–3.6 mHz bin (periodicity $P \approx 5$ min) and 6–8 mHz bin ($P \approx 2.5$ min). At right, all three curves peak near $r \approx 4$ arcsec.

The average presence of aureoles shows up as a power peak (bright) between $r = 3-7$ arcsec and $f = 5-7$ mHz.

Figure 16 displays the same power-versus-distance measurements for selected frequencies with spatial division between internetwork pixels, intermediate-category pixels, and their sum ("non-network") according to the mask definition in Fig. 4. The first panel illustrates that at low frequencies network power generally exceeds non-network power. The five-minute power distributions in the middle panel show a remarkable split between the intermediate and true internetwork pixels. Both categories display an initial dip followed by a rise of mean power with distance from the nearest network. The intermediate category does so at a much higher value.

The 6–8 mHz panel at right shows similar but steeper initial increases for all three pixel categories, peaks at $r = 3 - 5$ arcsec, and average decreases further out. The intermediate-category pixels provide the largest contribution to this pattern, also at large distance $r$. Thus, the high-frequency aureoles seem to favour the relatively large time-averaged brightness that make up the intermediate-category pixels – possibly marking the presence of persistent flashers, or the presence of overlying canopy fibrils as evidenced by the low-frequency C IV modulation map in Fig. 14.

Network shadows. Recently, Judge et al. (2001) have detected "magnetic shadows" in time-slice projections from SUMER measurements which they attribute to mode conversion in canopy fibrils (cf. McIntosh et al. 2001). In contrast to the power aureoles, these shadows are near-network areas that lack both in brightness and oscillatory power. Judge et al. (2001) plotted fractional modulation as defined by Eq. (4) which suggests that the shadows may correspond to the drop of the intermediate-category curve below the network one in the righthand panel of Fig. 13. Spatially resolved examples of such power normalisation are given in the top panels of Fig. 17, selecting the 5–min and 2.5–min frequency bands of the 1600 Å subfield that are shown in Fig. 14 without normalisation. The low power (darkness) of the network areas illustrates the relative lowering of the network curves from Fig. 12 to Fig. 13. These dark patches extend slightly beyond the brightest cores of the network (first panel of Fig. 4) and so overflow into our intermediate pixel category (light grey in the fourth panel of Fig. 4). Blinking these normalised-amplitude maps against the mean brightness maps shows that the dark patches correspond closely to the network at a somewhat less restrictive brightness contour, i.e. that their darkness derives primarily through the normalisation from the averaged network brightness. The aureoles quantified in Fig. 16 extend further and remain discernable as patchy bright borders in the upper-right panel.

Blinking the normalised-amplitude maps between wavelengths shows that the dark patches darken and grow with decreasing wavelength. This is illustrated with the second row of Fig. 17 which displays the 1550/1700 Å normalised-map ratio. Bright noise results from division by small numbers; greyish areas mark comparable
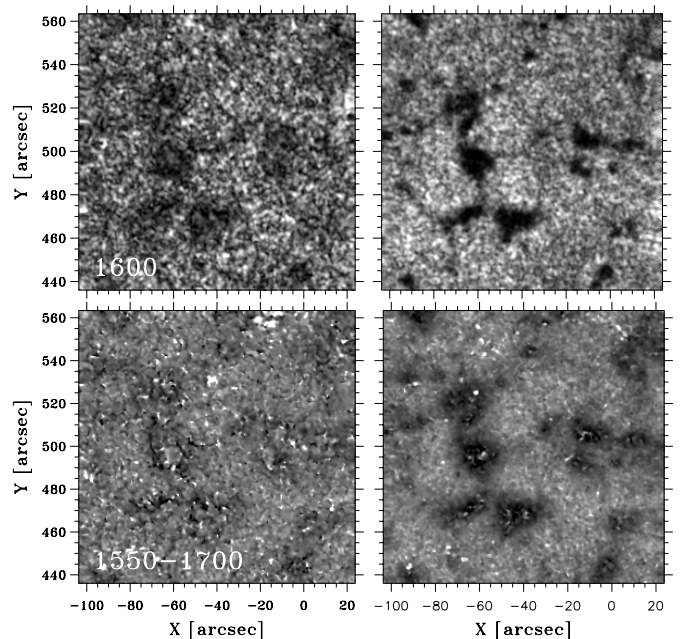


**Fig. 17.** Network shadows in normalised amplitude maps. Upper row: Fourier modulation maps for the top subfield of the 1600 Å May 12 data, similar to the third and fourth panels in the second row of Fig. 14 but with the greyscale representing linear Fourier amplitude per pixel normalised by the temporal mean per pixel. Lower row: ratio of 1550 and 1700 Å normalised amplitude maps. Left column: 2.6–3.6 mHz bin (periodicity $P \approx 5$ min). Right column: 6–8 mHz bin ($P \approx 2.5$ min).

modulation amplitude at the two wavelengths. The dark areas in the 2.5–min panel result from contrast increase with formation height, with appreciable dark-patch widening. The same areas darken slightly in the 5–min ratio map at left.

In the interpretation of Judge et al. (2001) the dark-patch increase should map magnetic canopy expansion with height as increasing loss of wave amplitude due to mode conversion, but it actually follows the growth of the temporal-mean network patches in the first column of Fig. 14 through the pixel-by-pixel normalisation. The apparent growth of the latter patches with formation height is indeed likely to mark canopy spreading, but the shadow behaviour in Fig. 17 cannot be attributed to mode conversion unless the wave amplitudes indeed scale with the mean brightness. Again, it is not clear a priori whether this is the case. Magnetic mode conversion seems better established at larger atmospheric height than sampled by the TRACE ultraviolet passbands (McIntosh et al. 2001).

### 4.3. One-dimensional modulation spectra

Figures 18–22 provide a variety of Fourier spectra in a compact format, showing power spectra, coherence spectra and phase-difference spectra for different pairs of diagnostics with spatial averaging split between internetwork and network through masks as in Fig. 4. We first discuss
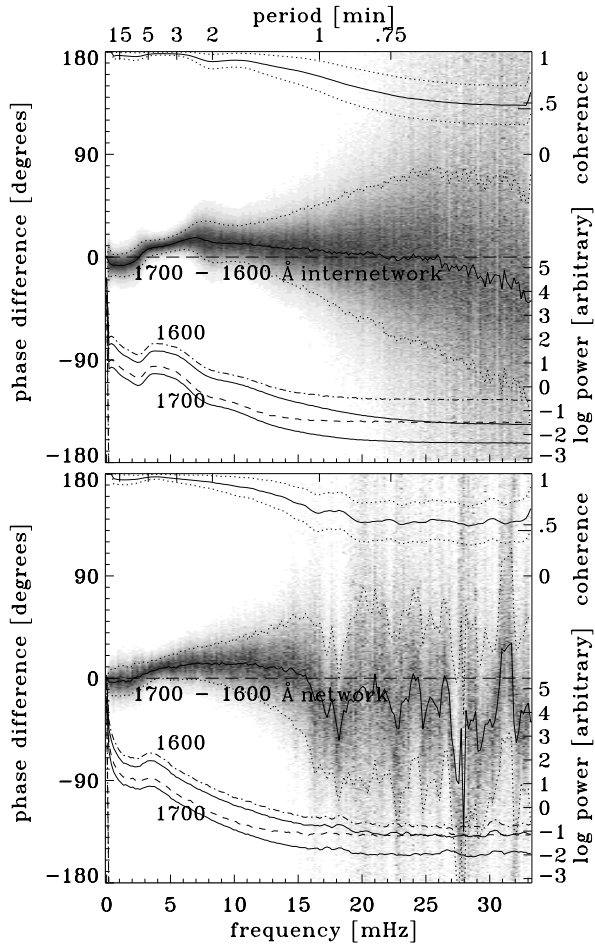
**Fig. 18.** Temporal Fourier spectra of the May 12 brightness data for 1700 and 1600 Å, spatially averaged over internetwork (upper panel, 7838 pixels) and network (lower panel, 37712 pixels). Abscissae: temporal frequency, corresponding periodicity specified along the top. Solid curves in the lower half of each panel: power spectra on a logarithmic scale (at right), with $1\sigma$ estimates (dash-dotted and dashed curves, the lower ones drop below the panel due to the logarithmic scaling). Solid curve in the upper half of each panel: coherence $C$ between 1700 and 1600 Å, with $1\sigma$ estimates (dotted; scale at right, the extra tick indicates the $C = 0.45$ random noise value). Scatter diagram in the middle of each panel: phase differences $\Delta\phi(1700-1600)$, scale at left, positive values corresponding to 1700 Å brightness leading 1600 Å brightness. Each spatial sample per frequency was weighted by the corresponding cross-power amplitude $\sqrt{P_1 P_2}$ and then binned into a greyscale plot normalised to the same maximum darkness per frequency bin (column). The solid curve is the spatial vector average defined by Eq. (7); the dotted $1\sigma$ curves are determined from the weighted phase differences. Pure noise produces $\Delta\phi$ scatter over all angles and correspondingly jagged behaviour of the mean $\Delta\phi$ curve.

Figs. 18–19 which are derived from the TRACE May 12 image sequences. Figure 18 compares 1700 Å brightness modulation to 1600 Å brightness modulation; Fig. 19 does the same for the 1600 Å and 1550 Å pair. The latter pair samples somewhat greater heights but the large similarity of the two figures indicates that the oscillations persist without major change of character over the increase.
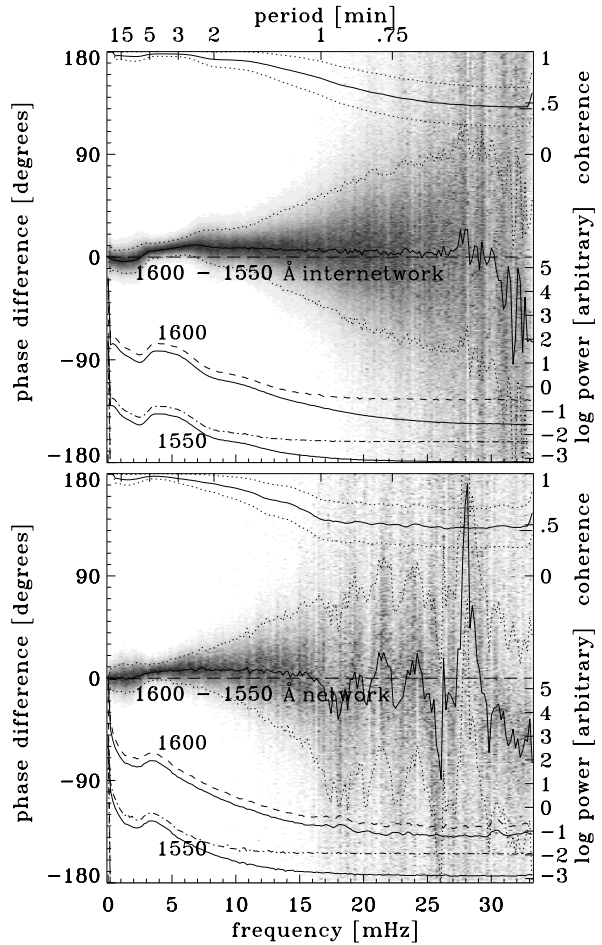
**Fig. 19.** Temporal Fourier spectra of the May 12 brightness data for 1600 Å and 1550 Å, spatially averaged over internetwork (upper panel) and network (lower panel). Format as for Fig. 18.

This is not the case for the Ca II H diagnostics shown in Figs. 20–22 from the data of Paper I simulated by CS1997, which again provide a useful comparison.

**Power and coherence.** The mask-defined spatial means of the temporal power spectra for each of the two passbands are shown at the bottom of each panel. They are the same as in Fig. 12 and are added here for reference, but now plotted on logarithmic scales to permit appreciation of the mean value and the high-frequency noise level. The units are the arbitrary TRACE data units. The same power spectra are shown with zero-frequency normalisation in Fig. 26. The combined network plus internetwork 1700 Å power spectrum is shown on a linear power scale in Fig. 23.

The mean brightness (zero frequency) and lowest-frequency modulation have much larger power than the acoustic oscillation peaks. The spectra show a gradual decline to the noise level at high frequency, with noisier behaviour of the network curves in the lower panel due to the smaller number of pixels.

The coherence $C$ between the members of each pair is plotted at the top of each panel, also with $1\sigma$ error estimates (scale at right). We remind the reader that

random noise gives $C = 0.45$ with our method of frequency averaging plus spatially independent sampling. The coherences are significant for $f < 15$ mHz in all panels of Figs. 18–19 and are very high in the 5–3 min band.

Phase differences. The phase-difference spectra are the most informative part of Figs. 18, 19. The pixel-by-pixel $\Delta\phi(x, y, f)$ values are shown as binned greyscale images in the format of Lites & Chipman (1979), weighting each $(X, Y, f)$ sample by the cross-power amplitude. The greyscale is scaled to the same maximum blackness for each frequency bin (column) in order to appreciate the spread also at low power. The spatial averages are obtained vectorially as defined by Eq. (7) in Sect. 2 and are plotted as solid curves through the scatter clouds, with $1\sigma$ curves determined from the weighted and binned distributions.

The spatial samples bunch up tightly in the acoustic oscillation band where the coherence is high, especially for the internetwork. The large amount of spatial sampling in our large-field image sequences yields very good statistics so that the average phase differences (solid curve) are very well determined in this band. At higher frequency the scatter increases. Note that pure random noise causes random scatter over all angles which does not average out to zero but produces equally erratic excursions of the average curves, with $1\sigma$ spread over 0.68 of the figure height. Such behaviour is seen at high frequency for the network averages, which are based on a smaller spatial sample.

The internetwork phase-difference behaviour in Figs. 18, 19 follows a well-defined pattern. It was observed earlier using optical lines (e.g., Fig. 7 of Lites & Chipman 1979; Fig. 7 of Lites et al. 1982; Fig. 7 of Paper I) and far-infrared continua (Kopp et al. 1992), but it is recovered here with much higher precision. At the lowest frequencies the internetwork shows a small but significant negative phase difference, meaning that the deeper-formed (longer wavelength) intensity lags the higher-formed intensity. This is attributed to internal gravity waves below. The 5-min oscillation ($f = 3.3$ mHz) has slightly positive $I-I$ phase difference due to radiative damping (comparable $V-V$ spectra as in the lower-left panel of Fig. 20 have zero phase difference as expected for evanescent waves). The phase difference then shows a gradual increase out to $f \approx 7$ mHz, implying upward acoustic wave propagation with the higher-formed 1600 Å brightness lagging 1700 Å brightness. The gradual increase follows the tilted line through $\Delta\phi = 0$ which would hold if the same height difference $\Delta h$ is sampled at each frequency and if all waves propagate up at the same speed $c_s$ so that $\Delta\phi = (\Delta h/c_s)f$ (cf. Lites & Chipman 1979). In this interpretation the increase has $\Delta h \approx 100$ km as characteristic value until $f = 7$ mHz where a slow decrease to $\Delta\phi = 0$ sets in. We return to this pattern after a comparison with Ca II H formation.

Comparison with Ca II H. It is again useful to compare our TRACE results with the Ca II H spectrogram sequence of Paper I. That analysis targeted network oscillations; Figs. 20–22 present unpublished but informative internetwork measurements from these data in a comprehensive Fourier format similar to Figs. 18, 19. Figure 20 displays wing modulation sufficiently far from H-line center to portray acoustic oscillations in the middle photosphere where they behave linearly in well-known fashion. Figures 21, 22 use the $H_{2V}$ brightness index which portrays nonlinear chromospheric kinetics in complex fashion. These figures bracket our TRACE data in formation height.

The upper panels of Fig. 20 compare $I-I$ internetwork Fourier modulation of the brightness in three blend-free spectral windows in the blue wing of Ca II H indicated by bars in Fig. 8. The oscillatory power peak becomes more pronounced at smaller separation from line center, i.e. higher formation. The $I-I$ phase-difference patterns are very similar to the phase-difference patterns in Figs. 18, 19.

The lower panels of Fig. 20 add Dopplershift analysis for the weakest Fe I blend in the Ca II H spectra, which is the line at $\lambda = 3966.82$ Å used by CS1997 to define their simulation piston. It samples height $h \approx 250$ km above the $\tau_{5000} = 1$ surface. The lefthand panel shows a $V-V$ comparison with the strongest Fe I blend in the Ca II H spectra (cf. Fig. 8) which was estimated to represent $h \approx 390$ km in Paper I from the phase difference at $f = 8$ mHz in this panel. The two power spectra have the same shape. Both lack the prominent low-frequency peak present in the brightness power spectra in the upper panels, but it should be noted that substantial spectrograph wavelength drift was removed from these Dopplershift measurements through nonlinear fit subtraction, a procedure which suppresses the small low-frequency peaks that do show up in the very similar (but more stable) data of Lites et al. (1994). The corresponding overshoot motions were therefore also not included in the simulation piston of CS1997, as shown by the piston power spectrum in Fig. 1 of Theurer et al. (1997a).

The $V-V$ phase-difference spectrum shows evanescent behaviour for the five-minute waves and again displays upward propagation at higher frequencies up to $f \approx 10$ mHz (blueshift is positive in this paper). The $V-V$ five-minute band shows very high coherence and a smaller spread than in the $I-I$ upper panels but the spread becomes slightly larger for the propagating regime because Dopplershift measurement is noisier.

The lower-right panel of Fig. 20 shows a $V-I$ comparison between Fe I 3966.82 Dopplershift and the Ca II H wing intensity at $\Delta\lambda = -1.36$ Å. Such $V-I$ comparisons usually assume that brightness represents temperature, Dopplershift measures velocity, and that the two sample the same atmospheric height for a given spectral line. These assumptions are often erroneous and can be very misleading (cf. Skartlien et al. 1994; Stein & Carlsson 1997); are they valid here? The Ca II H wing is not too much affected by coherent resonance scattering this far from line center (e.g., Uitenbroek 1989) and should obey LTE reasonably well, and the Fe I blends
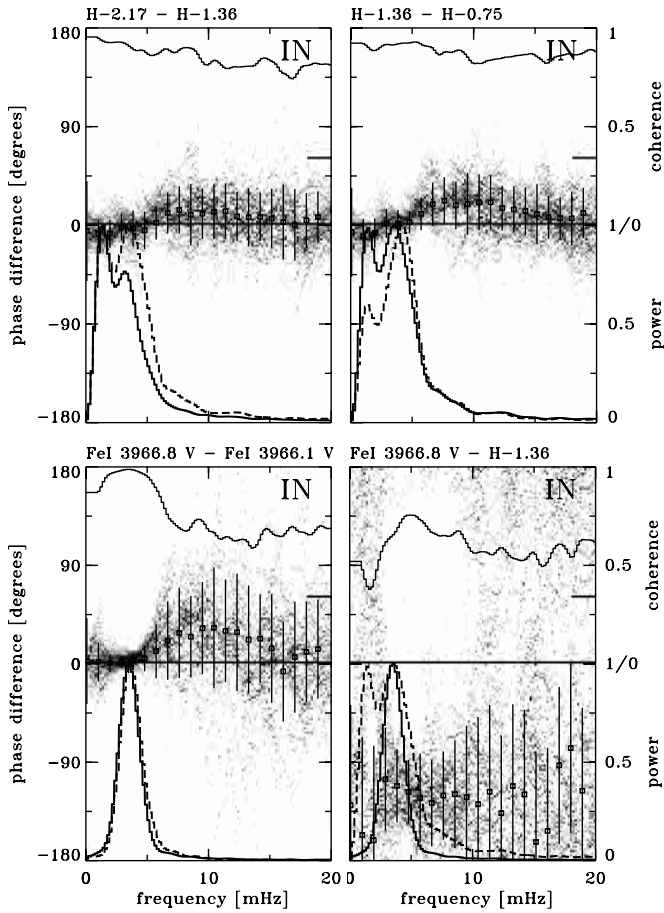
**Fig. 20.** Photospheric comparison Fourier spectra from the Ca II H data presented in Paper I. The format follows Lites et al. (1994) and is similar to that of Figs. 18, 19, but the power spectra (curves in lower half) are on linear scales normalised to their peaks with the mean removed, the coherence (curve in upper half) was evaluated with 9-point frequency averaging so that $C = 0.33$ for random noise (dash at right), the vector averages of the phase differences are shown as solid dots, and the $1\sigma$ estimates around the averages are plotted as bars. The lowest Dopplershift frequencies were removed in spectrograph drift correction ($V$ spectra in lower panels). The various diagnostics are indicated in Fig. 8, are formed well away from the H-line center, and are measured from internetwork only (IN). First panel: $I-I$ spectra for Ca II H wing brightness at $\Delta\lambda = -2.17$ Å and $-1.36$ Å from H center. Second panel: the same for wing brightness at $-1.36$ Å and $-0.75$ Å. Third panel: $V-V$ spectra for Fe I 3966.82 Å and Fe I 3966.07 Å Dopplershifts. Fourth panel: $V-I$ spectra for Fe I 3966.82 Å Dopplershift and wing brightness at $-1.36$ Å.

are also quite likely to have LTE source functions even when their opacity is depleted by radiative overionization (Athay & Lites 1972, cf. Rutten 1988). Figure 8 shows that the Fe I 3966.82 line core and the $-1.36$ Å wing window have the same spatially-averaged emergent intensity, which with LTE and the Eddington-Barbier approximation implies formation at the same average temperature and so at the same height. Indeed, their acoustic power peaks coincide and their phase differences are roughly constant with frequency. Thus, the classical assumptions do
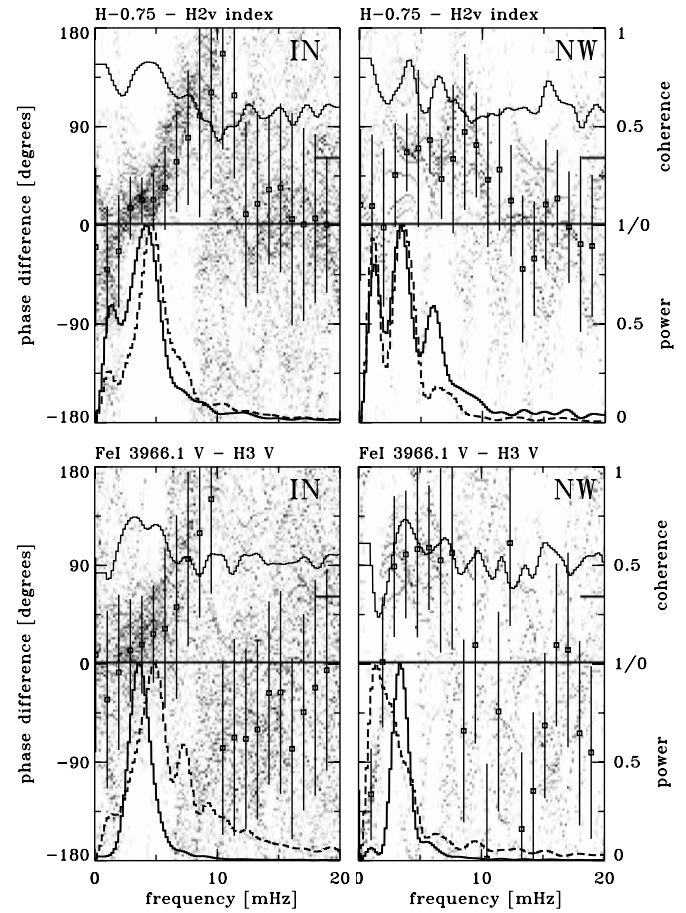
**Fig. 21.** Chromospheric comparison spectra from the Ca II H data discussed in Paper I in the format of Fig. 20. Left: internetwork. Right: network. Upper panels: $I-I$ spectra for wing brightness at $\Delta\lambda = -0.75$ Å and $H_{2V}$ index brightness. Lower panels: $V-V$ spectra for Fe I 3966.07 Å Dopplershift and Ca II $H_3$ line-center Dopplershift.

hold in this case. At the coherence peak at $f = 5$ mHz the $V-I$ lag of about $-120°$ fits the compilations from many lines in Figs. 1 and 3 of Deubner (1990) at the $h \approx 250$ km formation height and fits the classical interpretation of near-adiabaticity with some thermal relaxation (Schmieder 1976, 1977, 1978; Lites & Chipman 1979; Kopp et al. 1992).

Thus, all is well in Fig. 20. The TRACE Fourier spectra in Fig. 18 show comfortably similar $I-I$ behaviour with much better measurement statistics. Although the ultraviolet continua are not formed in LTE they apparently sample the same oscillations with similar height discrimination.

However, TRACE images and timeslices as in Figs. 5–7 display internetwork grains much like Ca II K filtergrams, so that comparison should also be made with Ca II H formation closer to line center. This is done in Figs. 21, 22. The upper panels of Fig. 21 show internetwork and network $I-I$ comparisons using the $H_{2V}$ brightness index of which the timeslice is shown in Fig. 9 and decomposed in Fig. 10. Its internetwork power spectrum is
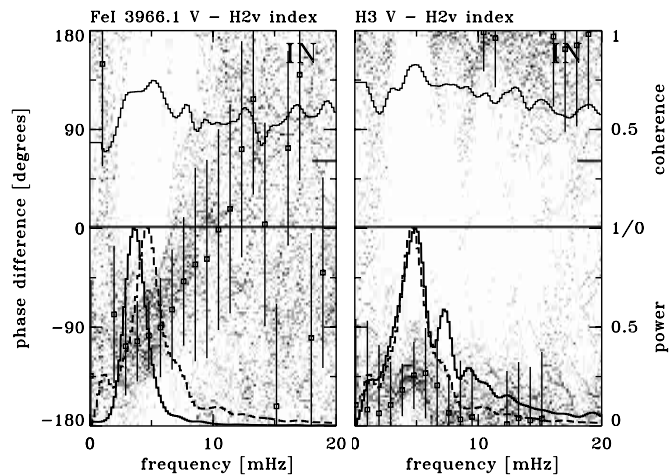
**Fig. 22.** Chromospheric $V-I$ spectra from the Ca II H data in Paper I for internetwork. Left: Fe I 3966.07 Å Dopplershift and $H_{2V}$ index. Right: $H_3$ Dopplershift and $H_{2V}$ index. The rms $\Delta\phi$ bars wrap around from below $-180°$ to above $+180°$ and vice-versa.

dominated by the $f = 5$ mHz peak and its phase differences with the $\Delta\lambda = -0.75$ Å brightness rise steeply with frequency, reaching $180°$ at $f = 10$ mHz. Spectrally, this upward propagation of the brightness modulation in the Ca II H & K wings was diagnosed from inward wing whisker contraction already by Beckers & Artzner (1974). It causes the fuzziness in the time direction of the $H_{2V}$ grains in the wide-band timeslice at right in Fig. 9. The steep $\Delta\phi(I-I)$ gradient across the three-minute band also contributes apparent dissimilarity between the two three-minute slices of Fig. 10 because it washes out timeslice structure with sampling height even at high coherence. The larger similarity of the internetwork parts of the two five-minute slices in Fig. 10 corresponds to constancy across the five-minute band of the total $\Delta\phi$ sum of the two righthand panels of Fig. 20 and the upper-left panel of Fig. 21.

The steep $\Delta\phi(I-I)$ increase is in conflict with the small amount of propagative difference in Fig. 19 if one assigns $H_{2V}$ brightness formation to temperature behaviour at temperature-minimum formation height. This would be the case if one assumes that equal time-averaged emergent intensity implies the same formation height, as proven above for the Fe I 3966.82 Å and $\Delta\lambda = -1.36$ Å pair. One would then assign Fe I 3966.82 Å and the $H_{2V}$ index to the same layer on the basis of their equal mean intensity in Fig. 8, but the assumption is wrong as indicated by the Fe I 3966.82 – Ca II $H_3$ $V-V$ comparison in the lower-left panel which shows a similar $\Delta\phi(f)$ gradient but spans a much larger height interval. The similarity illustrates that $H_{2V}$ brightness is strongly influenced by the Dopplershift excursions of the $H_3$ core well above the layer where the $H_{2V}$ photons escape, with $H_{2V}$ enhancements corresponding to $H_3$ redshifts. This well-known relationship, initially proposed and modelled by Athay (1970), Cram (1972), and Liu & Skumanich (1974), is explained in detail in the informative H-line formation break-down

diagrams in Figs. 4–7 of CS1997 and is here demonstrated observationally by the $V-I$ diagrams in Fig. 22. In the righthand panel the coherence is higher, the two three-minute power peaks are virtually identical, and $\Delta\phi(V-I)$ is roughly constant with frequency. Thus, the steep $\Delta\phi$ increases in the $I-I$ and the $V-V$ internetwork panels of Fig. 21 are both set by $H_3$ Dopplershift modulation. The same increase was observed in Fig. 5 of Lites & Chipman (1979) and the grain-rich $V-V$ diagram from 1991 data in Fig. 5 of Rutten (1994), and it is also present (with a sign-definition flip) in Fig. 4 of Skartlien et al. (1994) which evaluates $V-V$ phase difference for the Ca II $H_3$ – 8542 Å line pair from the CS1997 simulation, confirming that the increase is a characteristic of acoustic shock dynamics.

We conclude from this comparison that the internetwork Fourier behaviour diagnosed in Figs. 18–19 samples oscillations comparably to the inner wings of the Ca II H & K lines, but without the brightness enhancement that internetwork grains gain when observed at the $K_{2V}$ and $H_{2V}$ wavelengths from the large-amplitude shock modulation of the $H_3$ Dopplershift in higher layers.

**High-frequency waves.** Phase-difference measurements with TRACE should permit recognition of oscillation signatures to higher frequencies than is possible in ground-based observations. The interest in diagnosing high-frequency oscillations is large, for example to settle the current debate on chromospheric heating by high-frequency acoustic waves and their presence or absence in the Carlsson & Stein piston (Musielak et al. 1994; Theurer et al. 1997a; Theurer et al. 1997b; Ulmschneider 1999; Kalkofen et al. 1999) and its stellar ramifications (Cuntz et al. 1999).

The phase-difference spectra in Figs. 18, 19 show gradual decrease above $f \approx 7$ mHz. In older oscillation studies such declines have generally been attributed to atmospheric seeing (e.g., Endler & Deubner 1983; Deubner et al. 1984; Deubner & Fleck 1990; see Lites et al. 1994 for a discussion). In TRACE observations, however, there is no seeing apart from the small-scale guiding jitter that has mostly been removed by our alignment procedures. However, also from space acoustic oscillations are harder to measure at higher frequency because the wavelength shortens: at soundspeed propagation it drops to 350 km for $f = 20$ mHz. An upwards propagating wave may fit from maximum compression to maximum rarefaction within the response function width, so that much less power is detected than actually present – but even in that case phase difference may yet be measurable.

In this context the phase-difference behaviour for $f = 10 - 20$ mHz in the two lefthand panels of Fig. 21 should be noted. The noise is large (the $1\sigma$ bars nearly reaching their maximum extent of 68% of the panel height) but the averages seem to display a pattern which we deem possibly significant because similar behaviour is seen in Fig. 5 of Lites & Chipman (1979) and Fig. 7 of Rutten (1994).

Figures 18, 19 show no high-frequency behaviour analogous to the internetwork behaviour to Fig. 21 at all, only the gradual $\Delta\phi$ decrease. The latter seems significant even though the power drops strongly towards $f = 10$ mHz. We suggest that the phase difference decline results primarily from non-linear wave steepening. On their way to become weak acoustic shocks in the low chromosphere, the higher-frequency components travel faster and arrive earlier at the higher sampling location. In the TRACE brightness measurements the steepening is sampled far below the level that produces the patterns seen in Fig. 21, which must both be attributed to $K_3$ Dopplershift behaviour as discussed above. Thus, the $\Delta\phi$ decreases in Figs. 18, 19 sample nonlinear wave steepening at its onset, well below the level where shocks result and produce $H_{2V}$ and $K_{2V}$ grains as well as observable sawtooth behaviour. The question to what maximum frequency these $\Delta\phi$ decreases are significant is addressed in Sect. 5 where we conclude that the non-simultaneity of the TRACE imaging in the different passbands sets the $\Delta\phi$ reliability limit to $f = 15$ mHz at best.

**Network–internetwork differences.** The network panels in Figs. 18, 19 differ only slightly from the internetwork panels. The differences in power spectra are exhibited more clearly in Figs. 12, 13 and correspond to the relative lack of network power in the 2.5–min maps in Fig. 14. The coherences drop a bit faster with frequency in the network and the phase-difference scatter is slightly larger even in the five-minute band. The large similarity with the internetwork behaviour shows that the acoustic oscillations pervade network at these heights without much modification, as they do in the photosphere (plots as in Fig. 20 for network, not shown, are identical apart from small-sample noise).

The picture is drastically different for the chromospheric diagnostics in Fig. 21 where power spectra and phase difference behaviour are very different between network and internetwork. The fourth panel illustrates the conclusion of Paper I that the long-period modulation peak that is particular to chromospheric network sampled by $H_3$ Dopplershift has no connection (low coherence) to the dynamics of the underlying photosphere. This disconnection is demonstrated here by the large disparity in internetwork-network differences between Fig. 19 (upper and lower panels nearly the same) and Fig. 21 (left and right panels very different).

### 4.4. Two-dimensional modulation spectra

Figures 23, 24 complete our suite of Fourier diagnostics for the May 12 data in the form of two-dimensional power and phase-difference spectra, resolving the oscillations in both temporal frequency $f$ (vertical) and in spatial wavenumber $k_h$ through annular averaging over the horizontal $(k_x, k_y)$ plane. These spatially-averaged diagrams make no distinction between internetwork and network. Only the lower-left $(k_h, f)$ quadrants with significant structure are shown.
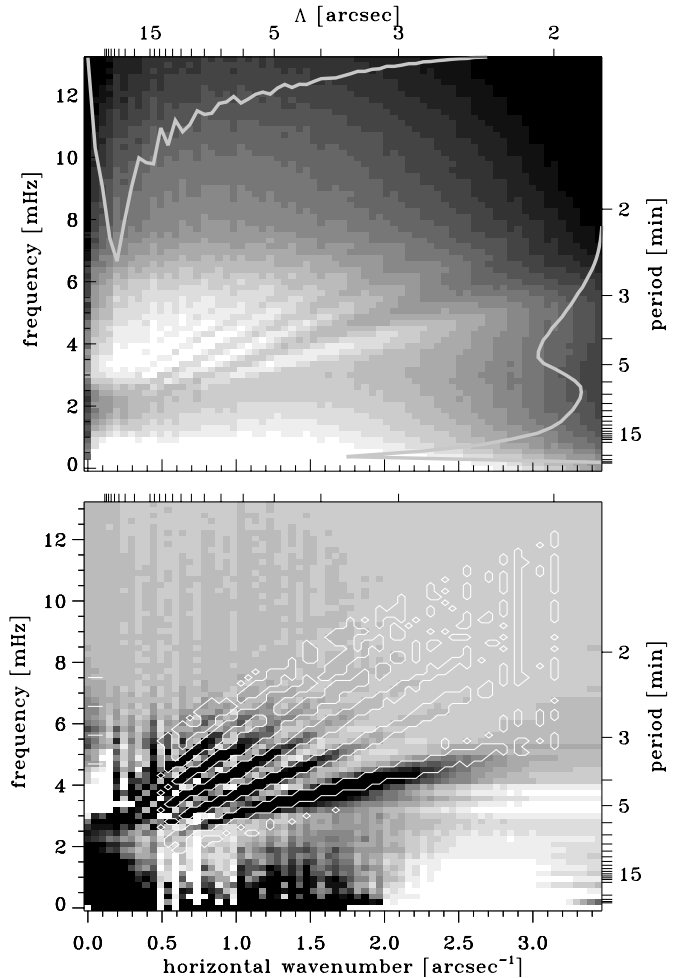


**Fig. 23.** Partial two-dimensional power spectra of the 1700 Å brightness in the complete May 12 sequence (full field and duration). Only the significant part is shown. Axes: horizontal wavenumber $k_h$ and temporal frequency $f$. The corresponding spatial wavelengths and temporal periodicities are specified along the top and at right. Upper panel: absolute brightness power on logarithmic greyscale. The solid curves show the temporally and spatially integrated power spectra on linear inverted scales with the mean and trend removed. Lower panel: the same after subtraction of the background variation to enhance the $p$-mode and pseudo-mode ridges, and with the greyscale inverted to display the contours better. The latter define the ridge mask. The vertical fringing is an artifact from TRACE data compression.

**Acoustic oscillations.** Figure 23 shows the $(k_h, f)$ power spectrum for the May 12 1700 Å data. The solid curves are the spatially and temporally averaged power spectra, respectively. The one at right is the combination of the internetwork and network 1700 Å power spectra in Fig. 18 but is here plotted on a linear scale with removal of the mean and trend to emphasise the low-frequency and acoustic modulation peaks.

The $(k_h, f)$ power spectrum contains $p$-mode ($f = 2$–5 mHz) and pseudo-mode (above the cutoff frequency $f_{AC} = 5.3$ mHz) power ridges out to $f = 8$ mHz and to $k_h = 3.2$ arcsec$^{-1}$ or spatial wavelength $\Lambda_h = 2$ arcsec
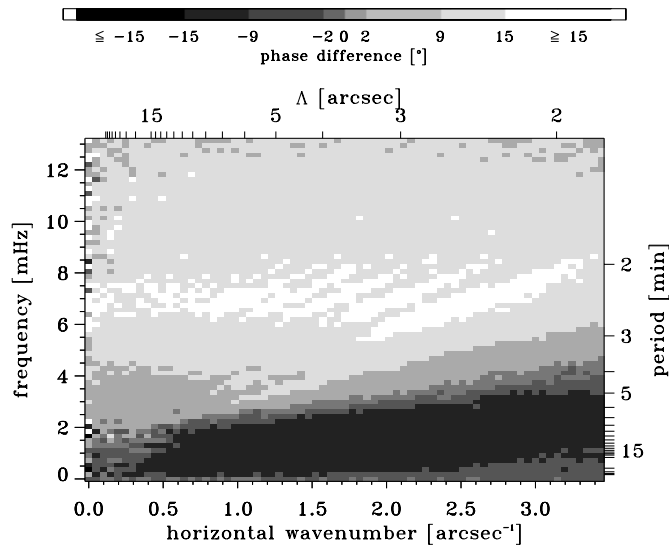
**Fig. 24.** Two-dimensional $\Delta\phi(1700-1600)$ phase-difference spectrum from the May 12 data. Axes: horizontal wavenumber $k_h$ and temporal frequency $f$. The corresponding wavelengths and periodicities are specified along the top and at right. Greyscale: phase difference $\Delta\phi$ coded as indicated at the top.
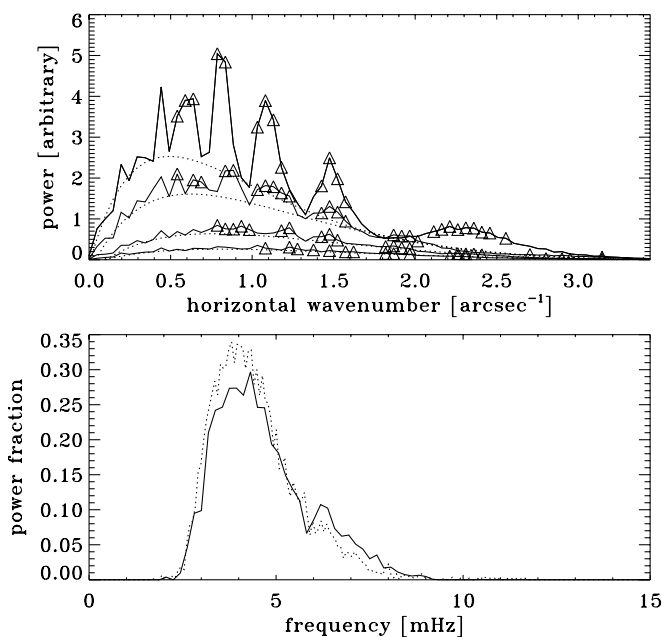


**Fig. 25.** Upper panel: absolute power in 1700 Å brightness as function of horizontal wavenumber at different frequencies, from top to bottom 4.7, 5.6, 6.6, 7.5 mHz. Triangles: ridge locations as in Fig. 23. Dotted curves: background estimates underlying the ridges. Lower panel: fraction of the summed ridge power (above the dotted backgrounds in the upper plot) of the total power, as function of frequency. The dotted curve results from the longer-duration October 14 sequence.

(scale on top; the latter limit may be set by the 1.5 arcsec boxcar image smoothing of the May 12 sequences). The pseudo-mode ridges do not originate from global mode selection through multi-pass interference, as is the case for the evanescent five-minute modes used in helioseismology,

but come from waves that are excited near the surface in downward directions and are reflected only once at the inward temperature increase before propagating upwards out of the photosphere. They add power to the directly excited outgoing wave at $(k_h, f)$ locations corresponding to the one-bounce travel length and duration from the source. Thus, they do not represent global wave interference but local power addition. They correspond to first-bounce power ridges in time-distance plots in which the appearance of only one ridge for three-minute waves established the up-and-out loss after the first reflection (Duvall et al. 1993), and they roughly obey the Duvall dispersion law for a fixed waveguide with $n$ nodes along its length (Duvall 1982; cf. Eq. (2.14) of Deubner & Gough 1984; see also Kumar et al. 1994; Kumar 1994; Jefferies 1998; Vorontsov et al. 1998).

Figure 24 shows the $(k_h, f)$ diagram for the May 12 1700−1600 Å phase differences. The pseudo-mode ridges stand out by having larger $\Delta\phi(1700-1600)$ values than between the ridges, representing a ridge-interridge split of the $\Delta\phi$ averages in Fig. 18. Since the ridges correspond to single-bounce power enhancements in $(k_h, f)$ selection, they are likely to correspond to locations where acoustic waves propagate vertically upwards. The on-ridge $\Delta\phi(1700-1600)$ values then correspond to vertical travel time between the two sampling heights for such waves. They do not stand out through interference between spatially different locations but because outward propagation is enhanced at the $(k_h, f)$ ridge locations.

The interridge background has smaller phase differences, implying partial non-propagative signature (oblique propagation would increase the delay). We suspect that these smaller differences are standing-wave contributions from partial reflections at larger height, possibly at shocks (e.g., Deubner et al. 1996; Carlsson & Stein 1999), or from deep penetration of ballistic post-shock downfall. In the Carlsson-Stein simulation, shocks are sometimes stopped in their upward propagation by such downdrafts after prior shocks. Such a case is observationally present in the form of the triple-grain sequence at the top of C+S Col. 30 ($x = 63$) in Figs. 9–11. When blinking the upper and lower rightmost panels of Fig. 10 against each other, the upward propagation of the three-minute waves is immediately evident as up-and-down jumping patterns – except for this particular grain train which appears standing still when blinked, so simultaneously present at the two sampling heights, with zero phase difference.

Not only does the interridge background have distinctly different phase behaviour at pseudo-mode frequencies but it also has appreciable power in the whole acoustic regime. This is quantified in Fig. 25. The upper panel shows power distributions along horizontal cuts through the $(k_h, f)$ diagram in Fig. 23. The ridges defined by the ridge mask (lower panel of Fig. 23) are indicated by triangles. The dotted curves are background estimations. The lower panel shows the fraction of ridge power above the local background summed over all mask ridges along horizontal cuts. The ridge power is most important below

the cutoff frequency but even there the background contribution is sizable. The latter rapidly gains importance with frequency above the cutoff frequency.

In the $p$-mode regime below the cutoff frequency the on-ridge power enhancements represent constructive interference of global oscillatons with long-duration mode persistence, whereas the $p$-mode background represents shorter-duration wavetrains from local excitations without global mode selection. Long-duration sampling as in helioseismology increases the ridge/interridge power contrast because shorter wavetrains then cancel through having random phases. In contrast, pseudo-mode ridges do not correspond to such long-duration persistence and may actually be dominated by local excitations, whereas the pseudo-mode background may have a larger interference contribution from wave reflections. This intrinsic difference is illustrated by the difference between the two curves in the lower panel of Fig. 25. The twice longer duration of the October 14 sequence (dotted curve) produces higher contrast for the $p$-mode ridges but lower contrast for the pseudo-mode ones.

Low-frequency oscillations. At lower frequency, the dark wedge in Fig. 24 indicates downward propagation which corresponds to the initial $\Delta\phi < 0$ dip in the upper panels of Figs. 18 and 20. The wedge shape, the location of the upper limit at the Lamb line, and the larger-than-granule wavelengths suggest strongly that this wedge is due to internal gravity waves (cf. Straus & Bonaccini 1997). It was previously observed in similar $(k_h, f)$ spectra from ground-based filtergram sequences by Kneer & von Uexküll (1993) who tentatively made the same identification, as did Schmieder (1976), Cram (1978), Brown & Harrison (1980), Deubner & Fleck (1989), Bonet et al. (1991) and Komm et al. (1991) from various other diagnostics. The same tentative identification was made in Paper I for the low-frequency power peaks shown here in Fig. 20. These are much higher, relatively to the acoustic peak, than the low-frequency Doppler modulation by convective overshoot (which is artifically suppressed in the lower panels of Figs. 20, 21 as noted above but remains well below the acoustic peak height in other data). We now confirm the identification as gravity waves from the $(k_h, f)$ phase-difference signature in Fig. 24.

It is no surprise to find gravity waves in the upper photosphere since they should be abundantly excited by convective overshoot. However, their detection is not easy because they combine long periods and short wavelengths with small Dopplershifts and because they travel preferentially in slanted directions, so that sampling widely different heights along radial lines of sight suffers loss of coherency (see the detailed descriptions and predictions in the fundamental papers of Mihalas & Toomre 1981, 1982).

Our TRACE $\Delta\phi(1700-1600)$ measurement represents a particularly sensitive gravity-wave diagnostic because *(i)* – it samples brightness rather than velocity, *(ii)* – does so sufficiently high (the intensity modulation grows considerably with height), but *(iii)* – yet below the wave breaking height above which the waves vanish, and *(iv)* – compares brightness phase at sufficiently close heights with sufficient spatial integration (1.5 arcsec boxcar smoothing) to detect slanted waves. The negative-phase signature is smaller for the higher-located sampling in Fig. 19; the corresponding $(k_h, f)$ diagram (not shown) has similar ridge-interridge difference at smaller amplitude.

The gravity wave signature is similarly present in the Ca II H wing brightness modulation spectra in the upper panels of Fig. 20, for the same reasons: gravity waves have much larger brightness modulation than Dopplershift modulation, the brightness modulation is sampled at heights where the amplitude grows large before reaching breaking height, and the Ca II H wing windows sample a sufficiently small height difference to avoid spatial mismatch from oblique propagation. In addition, since the H wings are formed in LTE they may respond more faithfully to temperature modulation than the ultraviolet continua which suffer from scattering. The low-frequency power peak is still weakly present in the internetwork $H_{2V}$ index spectrum in the upper-left panel of Fig. 21.

Note that both $H-0.75$ power and $H_{2V}$ index power have a (relatively) more pronounced low-frequency peak in the network (upper-right panel of Fig. 21) and that this peak seems to survive as the only peak in internetwork $H_3$ Dopplershift power (lower-right panel). The tantalising suggestion is that the $H_3$ Dopplershift peak may result from fluxtube interaction at mid-photospheric heights with gravity waves impinging sideways from the surrounding internetwork that get enhanced in the fluxtube. An alternative interpretation is that the network $H_3$ Dopplershift peak represents mottle flow dynamics as mapped by the second bottom panel of Fig. 14.

## 5. Error analysis

Comparison with October 14 data. For reasons of space we have only displayed results from the May 12 TRACE sequences so far. The October 14 sequences produce comparable timeslices, Fourier amplitude maps and Fourier spectra, with as major difference that the extreme quietness of the solar field makes the C IV construct yet more unreliable and dominated by noise. Nevertheless, the October 14 sequences provide a different sample that we use here to judge the reliability of the May 12 results, in particular the high-frequency parts of the Fourier spectra which are most sensitive to the nonsimultaneities and the cadence and timing irregularities of the TRACE image acquisition, which differ between the two dates.

Figure 26 compares Fourier spectra between the two dates in the format of Fig. 18 (but without scatter clouds and rms curves to avoid overcrowding). The power spectra are again plotted logarithmically but are now made comparable by zero-frequency normalisation as in Eq. (4). The October 14 power spectra have a higher noise level at high frequency. The acoustic peaks are about the same for the two dates.
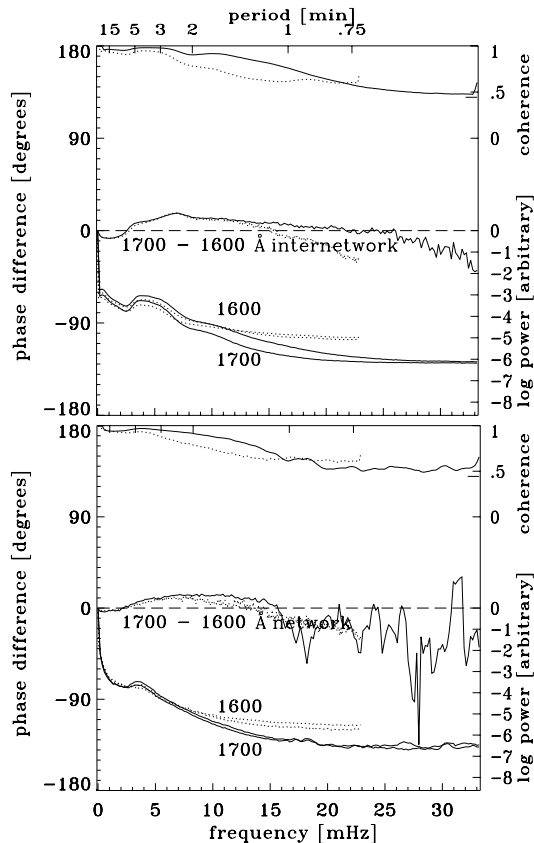
**Fig. 26.** Comparison of the spatially averaged Fourier spectra from May 12 1998 and from October 14 1998. The solid curves are the same as in Fig. 18 except that the power spectra are normalised to the zero-frequency value (square of the mean intensity). The October 14 spectra are dashed and have a lower Nykvist frequency (23 mHz).

The phase-difference averages differ much between the two dates from $f \approx 15$ mHz onwards, even in the well-sampled internetwork (upper panels). The averaged coherences disagree appreciably at even lower frequency.

The TRACE fields sample a sizable fraction of the solar disk. The October 14 field was even quieter than the May 12 field but there is no reason to assume that the internetwork was intrinsically different between the two dates in these large spatial averages. Thus, we may expect the solar behaviour to have been similar at the two dates (except for the C IV construct), especially in the internetwork. The fact that the mean phase difference and coherence spectra differ so much above $f \approx 15$ mHz implies that measurement errors and measurement differences are important and upset our anticipation of diagnosing high-frequency oscillation properties exploiting the TRACE virtues of seeing-less and statistically-rich sampling. Various tests were therefore made to elucidate these errors. The principal question is to what frequency the phase-difference spectra are reliable.

**Phase-difference closure.** A direct reliability test of the phase differences in Figs. 18, 19 is available in the form of phase-difference closure. If each passband samples a well-defined oscillation phase per frequency, the
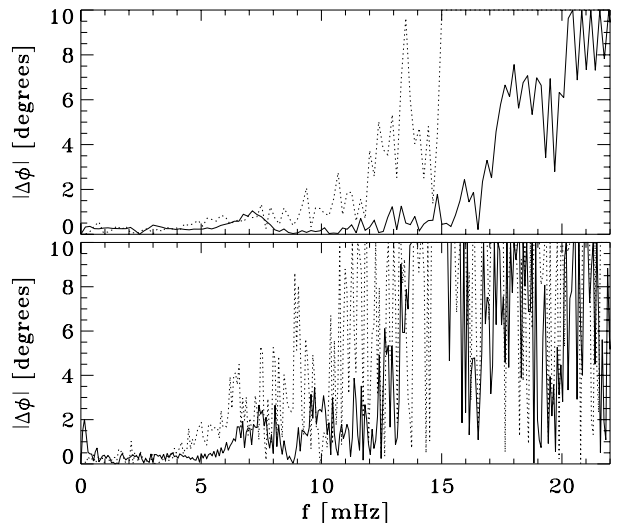


**Fig. 27.** Phase-difference closure. The curves show $|\Delta\phi(1700{-}1600) + \Delta\phi(1600{-}1550) - \Delta\phi(1700{-}1550)|$ where each $\Delta\phi$ is the vector-averaged mean phase difference (solid curves in Figs. 18–19). Solid: internetwork. Dashed: network. Upper panel: May 12 data. Lower panel: October 14 data.

$\Delta\phi(1700{-}1550)$ differences should equal the summed $\Delta\phi(1700{-}1600)$ and $\Delta\phi(1600{-}1550)$ values. Figure 27 shows that the direct and summed evaluations depart between $f = 10$ and $f = 15$ mHz, and for the network at somehat lower frequencies. This is the same frequency region in which the phase-difference spectra in Fig. 26 depart from each other, indicating that the averaged phase-difference spectra in Figs. 18, 19 indeed become unreliable in this frequency band.

**Window taper.** In standard practice, the 10% start and end segments of the brightness sequence per pixel were multiplied by a 10% cosine bell taper to the mean value in order to suppress window edge effects. The original mean was restored as zero-frequency amplitude after the transform. Tests changing or even deleting the edge taper produced more high-frequency noise as expected from edge discontinuities (Brault & White 1971), but no significant change in phase-difference behaviour.

**Discrete sampling.** TRACE has no high-frequency filter to suppress noise above the Nykvist frequency. The power curves in Fig. 18 still decrease slightly close to the Nykvist frequency, so that some aliasing seems indeed to occur. However, the Nykvist frequency is quite high in the May 12 data. The power spectra are appreciably higher around $f = 15$ mHz so that the phase-difference spectra should be dominated by non-aliased signal around this frequency. However, at higher frequencies the sampling itself becomes inadequate for phase measurements below the Nykvist frequency. These imply a three-parameter sinusoidal fit (amplitude, offset, and phase) to each signal per frequency and pixel, so that the uncertainties increase rapidly when the signal is sampled less then 3 times per period, i.e. above $f \approx 17$ mHz for the May 12 data.
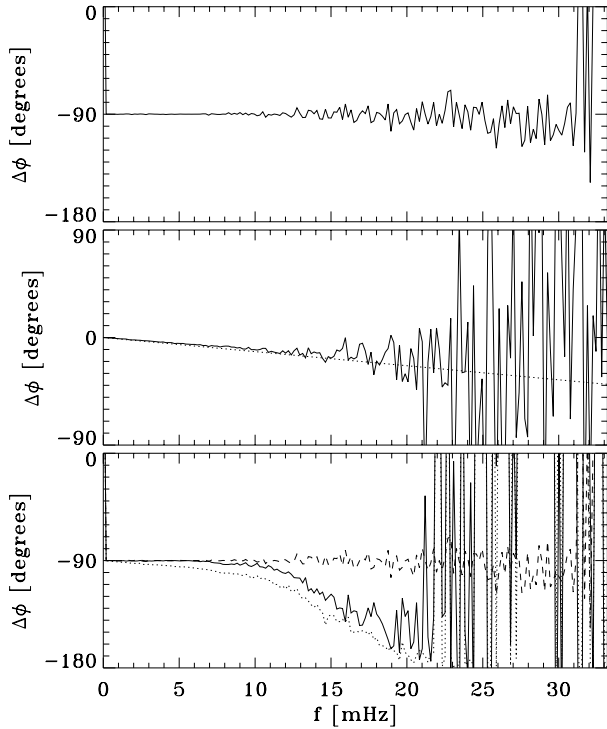
**Fig. 28.** Phase-difference tests using 2500 pairs of artificial solar-like signals with random phase per frequency in the first signal. The top panel results when the second signal is identical to the first one apart from a phase delay of $-90°$ per frequency and both are sampled simultaneously with the actual TRACE 1600 Å timing sequence. The solid curve in the middle panel results when the two signals are identical (without phase delay) but are sampled TRACE-like with the 1600 and 1700 Å timing sequences, which have an average offset of 5 s. The dotted curve shows the phase difference for a constant offset of 5 s between signals. The dotted curve in the bottom panel shows the combination (two signals $-90°$ out of phase sampled TRACE-like). The solid curve includes correction for constant 5 s offset and emulates our phase difference evaluations from the actual data. The curve in the top panel is overlaid for comparison.

Non-simultaneous sampling. The worst phase-difference error source is the non-simultaneity of the imaging in the different passbands. In principle, the temporal offset between the samples in two sequences introduces phase difference at each frequency that equals the offset divided by the period, a linear increase with frequency that was corrected using the equidistant time scale defined for each dataset. (The correction also makes $\Delta\phi$ depart from $0°$ or $\pm180°$ at the Nykvist frequency.) However, the actual timing irregularities and exposure durations cause uncertainties that also increase with frequency and become quite large at the high-frequency end – as demonstrated below.

Sampling tests. Figure 28 illustrates the effects of the major sampling errors on phase-difference measurements by using an artificially generated signal that possesses a solar-like power spectrum. Statistical variation was introduced by generating 2500 realizations in each of which the phase was chosen randomly at each frequency. The top

panel illustrates errors due to discrete sampling and sampling irregularities alone. It uses the actual mid-exposure timing sequence of the May 12 1600 Å data to measure phase differences between the 2500 artificial signals and 2500 copies that are phase-shifted over $-90°$ at each frequency. The curve shows the result from vector-averaged phase-difference determination as done above. The deviations from $\Delta\phi = -90°$ illustrate the errors caused by the non-equidistant exposure timing. They are reasonably small out to high frequencies.

The middle panel of Fig. 28 shows a similar test using 2500 pairs of identical (not phase-shifted) signals sampled with the actual 1600 and 1700 Å timing sequences. The noise increases considerably compared with the top panel.

The bottom panel results from a 2500-pair test combining the two error sources. It indicates that the irregular sampling of different signals at unequal times introduces large errors that cause appreciable $\Delta\phi$ distortion for frequencies above $f = 10$ mHz and large $\Delta\phi$ scatter above $f = 20$ mHz. The phase closure test in Fig. 27 indicates a somewhat larger extent of reliability, out to $f = 15$ mHz for errors below $10°$, in the internetwork which provided more samples than the 2500 used in these tests. The internetwork $\Delta\phi$ curves in Fig. 26 also show equality up to $f = 15$ mHz.

The conclusion is that, even though the TRACE data do not suffer from seeing, the sequential nature of TRACE's filter-wheel switching between passbands combined with the sampling irregularity is the major contributor of phase-difference noise and limits the reliability of the $\Delta\phi$ spectra in Figs. 18, 19 to frequencies below $f \approx 15$ mHz.

## 6. Discussion

Acoustic oscillations. A major supplier of dynamics in the internetwork atmosphere at the heights sampled by TRACE's ultraviolet passbands is, obviously, the so-called chromospheric three-minute oscillation, i.e. the broad peak for 2–5 min periodicity in the spatially-averaged power spectra in Figs. 12, 13 and 23. The fast-changing "sea of motion" sampled by the cutouts in Fig. 5, the dappled appearance of the internetwork parts of the timeslices in Fig. 7, the tight concentration of the three-minute $\Delta\phi$ spread in Figs. 18, 19, and the amount of three-minute power in Fig. 12 all attest to this ubiquitous oscillation gaining dynamical dominance already in the upper photosphere. There is not much else happening at these heights for frequencies around $f = 5$ mHz or the coherences wouldn't be so high and the $\Delta\phi$ spreads wouldn't be so small.

Our extensive comparisons with comparable displays from the Ca II H data of Lites et al. (1993) in Figs. 9–11 and Figs. 20–22 show that the ultraviolet continua sample the upper photosphere and low chromosphere rather like the inner wings of Ca II H, but without the higher-up Dopplershift effects of $H_3$ that produce the spectral asymmetry and intricate time-dependent spectral variations of

the H & K emission reversals. Since the spectral Ca II H behaviour in these very data was convincingly reproduced by the simulations of CS1997, we deem it beyond doubt that the highly similar internetwork behaviour in the ultraviolet timeslices and Fourier spectra is set by acoustic waves that are steepening into weak shocks on their way up. As discussed in Sect. 4.3, we suspect that the mean $\Delta\phi$ decline in Figs. 18, 19 from $f \approx 7$ mHz to $f \approx 15$ mHz (where $\Delta\phi$ becomes unreliable) results at least partially from wave steepening. We suspect also that similar phase-difference declines in older ground-based data were also partially due to wave steepening rather than atmospheric seeing.

Many of our results, in particular the phase differences in Figs. 18–19, are amenable to radiation-hydrodynamics simulations as those of Skartlien et al. (1994). Compared to their Ca II H modelling, the lower heights of formation of the ultraviolet continua (implying smaller sensivity to canopy geometry) and the more straightforward computation (no sensitivity to unidentified microturbulence or to coherency in resonance and Raman scattering) warrant the expectation that such numerical modelling should reproduce our observations in considerable detail. The major obstacle might be the one-dimensionality of the Carlsson-Stein approach, but it should be noted that the spatial extent of the time-compressed internetwork features in the lower panel of Fig. 11 is appreciably larger than the pixel size; column shifts of 1–2 arcsec (700–1500 km) sample scene differences primarily in the form of phase shifts, whereas the radial stratification varies much more rapidly.

The ongoing debate on the presence or absence, both in the Carlsson-Stein Ca II H simulation and in the real Sun, of a sizable heating contribution by high-frequency waves (e.g., Kalkofen et al. 1999) is not decided by our data. Our initial expectations were that phase differences should provide the clearest signature of high-frequency oscillations in the presence of much larger power at lower frequencies, and that the ultraviolet continua, which are formed at heights where wave amplitudes grow and steepen but are not yet disturbed by magnetic canopies, should provide the best diagnostic. Our hope was that TRACE's seeing-free and large-sample data gathering would unequivocally settle this issue – but we did not anticipate that the sequentiality of TRACE's imaging in different passbands upsets phase difference measurements as far below the Nykvist frequency as shown in Sect. 5. Of course, the wide contribution functions of the ultraviolet continua (sampled by TRACE with very wide passbands), the reduced sensitivity to thermal modulation caused by resonance-like bound-free scattering in these continua, and slowness of the pertinent recombination rates may together cause low modulation sensitivity and so limit the detectability of high-frequency phases. Numerical simulations can assess which waves may leave what signature in TRACE-like data and indicate up to what frequency waves are at all observable with future (or ideal) instruments.

Excess sound emission from collapsing granules (Skartlien 1998; Rast 1999; Skartlien et al. 2000), in intergranular lanes within mesoscale convergence areas (Hoekzema & Brandt 2000) and in acoustic flux events (Goode et al. 1998) as well as wave refraction (Hoekzema et al. 1998b; Stix 2000) are likely to contribute some mapping of granular dynamics into the acoustic modulation pattern. For oscillations with long-duration persistence as the global $p$-modes, the signatures of local excitations are largely – if not fully – lost in the many-wave and multi-pass interference that produces the wavy-curtain five-minute timeslice patterns (e.g., Fig. 9), but above the cutoff frequency the pseudo-mode ridges are mostly due to single-bounce enhancement so that more of the excitation pattern may remain. However, the rapid apparent motions of the brightness modulation along the background-mesh strands and the timeslice patterns in Figs. 9–11 strongly suggest wave interference as the major acoustic patterning agent. The acoustic piston studies listed above indeed rely on extensive spatial averaging to identify collapsing granules and mesoscale convergence as sites of enhanced acoustic wave excitation. Apparently, direct one-to-one mapping of individual pistons to resulting wave trains is made impossible by the ubiquitous wave spreading and interference.

Low-frequency modulation. The three-minute acoustic oscillation appears as modulation of the background mesh pattern seen in the reversed-greyscale panels in Fig. 5 and as columnar structures in the compressed timeslices in Fig. 11. This background pattern corresponds to the pronounced low-frequency modulation peak in the spatially-averaged power spectra in Fig. 12 and Fig. 23. It is likely to be a complex mixture of granular overshoot dynamics, internal gravity waves, and the low-frequency tail of acoustic interference patterns as those evident in the photospheric five-minute Doppler timeslice in Fig. 10. However, on the basis of the well-defined negative-phase signatures in Figs. 18 and 24, we believe that internal gravity waves are the principal constituent and that the mesh pattern primarily portrays their spatio-temporal interference. Further analysis adding the October 14 white light sequence confirms this view and will be reported in a future paper.

Internetwork grains. The physics of spectral $K_{2V}$ grain formation has been explained by CS1997 but the spatial patterns in which grains appear are not directly amenable to such one-dimensional simulation. The latter ascertained that acoustic three-minute waves are the principal grain-causing ingredient, but our results suggest that an important additional contribution comes from the slowly-varying background mesh which we attribute to internal gravity waves. The dominance of the two corresponding power peaks in Figs. 12, 13, the well-defined phase relations in Fig. 18, and the consistent grain-to-mesh superposition observed in movies and shown by Fig. 11 suggest that these two constituents together dominate

internetwork grain occurrence. Thus, we conclude once again that internetwork grain patterns are set primarily by wave interference with the brightest grains resulting from constructive additions (e.g., Rutten & Uitenbroek 1991a; von Uexküll & Kneer 1995; Judge et al. 2001), but we now add the gravity-wave background as extra occurrence agent.

Neither the acoustic-wave nor the gravity-wave interference patterns should be regarded as pistons, but rather as modulations that combine to define grain appearance. The combining explains the grain-mesh correlation, the apparent travel along mesh strands seen in the TRACE movies, and the frequent appearance of grains in close pairs and clusters outlining the mesh pattern. Note that the combining is nonsinusoidal through the nonlinear temperature sensitivity of the Planck function in the ultraviolet and the onset of wave steepening at these heights.

The actual pistons are to be sought in collapsing, exploding, and/or overshooting granules, or other convective generators of acoustic events and gravity-wave emission. As noted above, such searches are effectively hampered by the ubiquitous interference of the resulting waves. Acoustic waves preferentially propagate straight up but gravity waves propagate downward and spread under large angles with the vertical (Mihalas & Toomre 1981, 1982).

As shown in Sect. 4.3, the internetwork grains also sense higher-up Dopplershifts when observed in optically thick lines such as H & K (Figs. 21, 22). The ultraviolet continua provide a cleaner picture, but we should note that the time-dependent spectral asymmetry introduced by $H_3$ Dopplershifts to $H_{2V}$ grain evolution did provide a suitable yardstick to gauge CS1997 simulation success.

Network waves. The modulation spectra in Fig. 12 and the modulation maps in Fig. 14 once again confirm that network harbours low-frequency rather than high-frequency motions. The lower panels of Figs. 18, 19 show no distinctive network properties as those seen higher up (Fig. 21). Note that observed wave amplitudes may also be reduced by phase mixing between different fluxtubes within a cluster making up a network patch; Fourier studies of single-element flashers may provide a tactic to isolate fluxtube wave modes.

At low frequencies there is no sign of distinctive peaks in the network power spectra in Figs. 18, 19 as the one at 2.5 mHz in the $H_3$ Dopplershift spectrum in Fig. 6 of Paper I, which was taken as significant and attributed to kink-wave cutoff by Hasan & Kalkofen (1999). Such peaks are absent in the fourth panel of Fig. 21 which is produced from the same data with somewhat different averaging and smoothing choices. Our TRACE data provide far better statistics, so that we conclude that specific network modulation peaks that might suggest specific fluxtube wave modes have not really been detected so far.

On the other hand, the ubiquitous presence of internal gravity waves indicated by the low-frequency power and phase-difference behaviour in Figs. 18, 23, 24 and the coupling to fluxtube modes suggested by the low-frequency

peak equality in Fig. 21 may signify the importance of fluxtube interaction with internal gravity waves. The lack of coherence between $H_3$ and Ca I 4226.7 Å Dopplershifts in network led to the conclusion in Paper I that the slow network modulation is not correlated with underlying photospheric disturbances. A similar lack of $V-V$ coherence is seen in the fourth panel of Fig. 21. However, the $I-I$ comparison in the second panel has low-frequency network peaks for both signals, with larger coherence between them. The absence of a comparable Dopplershift connection may be due to the smallness of gravity-wave velocity perturbations compared to brightness perturbations.

Alternative explanations of the large low-frequency modulation in network are (i) – slow footpoint motions as suggested by Kneer & von Uexküll (1985, 1986), and (ii) – that the canopies spreading out from fluxtubes funnel gravity waves down as suggested by Deubner & Fleck (1990), but their interpretation of phase differences between the Ca II infrared lines suffers from non-trivial response characteristics of these lines (Shine & Linsky 1974; Rutten & Uitenbroek 1991a; Skartlien et al. 1994). As noted above, alternative explanations for the slow Ca II $H_3$ Doppler modulation in network are also such slow footpoint motions, or mottle flow changes as observed in C IV. The latter ones would have to also affect deeper fluxtube parts to cause the low-frequency brightness modulation enhancements in Fig. 12.

Intermediate zones. Two unexpected findings are the wide zones of intermediate-brightness pixels between network and "true" internetwork in Fig. 4 and the appearance of mottle-like structures surrounding network in low-frequency C IV modulation maps (Fig. 14). In older Ca II K filtergram sequences we have also noted wide zones of somewhat enhanced emission around network, but at the time suspected atmospheric seeing and telescopic straylight as main cause. The C IV modulation maps indicate that these zones are low-lying magnetic canopies rather like the fibrils that fan out from network on Hα movies, as discussed in Sect. 4.2. These zones may be brighter in ultraviolet continua due to smaller opacity. There may also be a time-averaged brightness enhancement from a larger density of single-fluxtube magnetic flashers, or there may be more wave dissipation in the network neighbourhood.

Network modulation aureoles. The same zones appear as enhanced three-minute modulation aureoles in the fourth column of Fig. 14. Hindman & Brown (1998) proposed that the absence of brightness modulation aureoles in their photospheric MDI data implies incompressible waves, and that the Ca II K brightness on the image sequences of Braun et al. (1992) was contaminated by Dopplershifts. Such contamination is indeed illustrated by Figs. 21, 22, but the aureoles in our TRACE continuum brightness data sample intrinsic brightness modulation resulting from temperature and/or opacity variations, not Dopplershifts. However, even the decidedly acoustic waves that make up Ca II $K_{2V}$ grains quickly loose their brightness signature

with height, whereas their Doppler signature persists (e.g., Cram 1978; Carlsson et al. 1997; Doyle et al. 1999). Intensity is formed with much more complexity than Dopplershift (in which the last particle-photon interaction does the coding) in any non-LTE situation; we note once more that the ultraviolet continua are affected by scattering similar to two-level-atom resonance scattering. Thus, non-existence of brightness aureoles would not prove wave incompressibility. The slight but definitely present brightness-modulation aureoles in (Figs. 14–16) point to some compressibility. We suspect that they are basically acoustic.

## 7. Conclusions

We have used ultraviolet image sequences from TRACE to provide a detailed view of quiet-Sun brightness oscillations in the upper photosphere and low chromosphere. The view is made comprehensive through combining space-time and Fourier representations of various sorts and through comparison with the well-modelled spectral behaviour of Ca II H. The view is also well-defined because the ultraviolet passbands yield a simpler picture than the Dopplershift-sensitive Ca II H core and are not too sensitive to magnetic canopy variations, and because TRACE's image sequences co-align precisely, do not suffer from seeing, and provide excellent statistics by combining large field with long duration.

A major motivation for this study was to diagnose high-frequency waves (well above $f = 10$ mHz) that might heat the internetwork and network chromospheres. We have not found those, but instead have detected:

- Well-defined acoustic phase-difference properties between different passbands including signatures of wave steepening (Figs. 18, 19).
- Phase-difference contrast between the $p$-mode and pesudo-mode ridges and the interridges in two-dimensional $(k_h, f)$ phase-difference spectra (Fig. 24).
- Strong evidence for ubiquitous internal gravity waves (Figs. 18 and 24).
- A mesh background pattern to the three-minute oscillation, which we attribute primarily to gravity-wave interference (Figs. 5, 11). The spatio-temporal appearance of internetwork grains is dominated by constructive interference between the acoustic and gravity wave patterns (Fig. 11).
- Three-minute brightness modulation aureoles around network (Figs. 14–16).
- Narrower modulation shadows around network – but only when normalised by the mean brightness (Fig. 17).
- Frequent presence of "persistent flashers", network-like features "on the loose" that presumably have magnetic anchoring and seem to represent isolated flux-tubes (Fig. 9).
- Wide zones of "intermediate" pixels between network and internetwork that have higher time-averaged brightness than the internetwork "cell" centers (Fig. 4). They contain more flashers and correspond closely to the mottle-like extensions seen in low-frequency C IV modulation which presumably delineate low-canopy topology (Fig. 14).

These findings define obvious desires for further study. Some issues, such as the properties and nature of power aureoles and the effects of canopy geometry, will gain from sampling more solar scenes in similar fashion but with variety in the degree of activity. The role of granular dynamics in setting the acoustic oscillation and the background mesh patterns may be studied through combination with photospheric imaging and Doppler mapping, by TRACE and MDI or with ground-based telescopes at higher angular resolution. The persistent flashers may be identified and studied using high-resolution magnetograms. The phase relationships portrayed here provide a valuable testbed for numerical simulation of the chromospheric three-minute oscillation. Internal gravity waves will be explored in a future paper using the October 14 white light data. Finally, simultaneous passband sampling as envisaged for the *Solar Diagnostics Observatory* may push the phase detectability limit to higher frequencies than reached here.

## References

Athay, R. G. 1970, Sol. Phys., 11, 347
Athay, R. G., & Lites, B. W. 1972, ApJ, 176, 809
Beckers, J. M., & Artzner, G. 1974, Sol. Phys., 37, 309
Berger, T. E., Löfdahl, M. G., Shine, R. S., & Title, A. M. 1998, ApJ, 495, 973
Bonet, J. A., Marquez, I., Vázquez, M., & Wöhl, H. 1991, A&A, 244, 492
Bonnet, R. M., Bruner, M., Acton, L. W., et al. 1982, A&A, 111, 125
Brandt, P. N., Rutten, R. J., Shine, R. A., & Trujillo Bueno, J. 1992, in Cool Stars, Stellar Systems, and the Sun, Proc. Seventh Cambridge Workshop, ed. M. S. Giampapa, & J. A. Bookbinder, ASP Conf. Ser., 26, 161
Brandt, P. N., Rutten, R. J., Shine, R. A., & Trujillo Bueno, J. 1994, in Solar Surface Magnetism, ed. R. J. Rutten, & C. J. Schrijver, NATO ASI Ser. C 433 (Kluwer, Dordrecht), 251

Brault, J. W., & White, O. R. 1971, A&A, 13, 169

Braun, D. C., & Lindsey, C. 1999, ApJ, 513, L79

Braun, D. C., Lindsey, C., Fan, Y., & Jefferies, S. M. 1992, ApJ, 392, 739

Brown, T. M., & Harrison, R. L. 1980, ApJ, 236, L169

Brown, T. M., Bogdan, T. J., Lites, B. W., & Thomas, J. H. 1992, ApJ, 394, L65

Brueckner, G. E. 1980, Highlights of Astronomy (IAU), 5, 557

Carlsson, M. 1999, in Magnetic Fields and Solar Processes, Proc. 9th European Meeting on Solar Physics, ed. A. Wilson, ESA SP-448 (ESA Publ. Div., ESTEC, Noordwijk), 183

Carlsson, M., & Stein, R. F. 1992, ApJ, 397, L59

Carlsson, M., & Stein, R. F. 1994, in Chromospheric Dynamics, Proc. Miniworkshop, ed. M. Carlsson, Inst. Theor. Astrophys., Oslo, 47

Carlsson, M., & Stein, R. F. 1995, ApJ, 440, L29

Carlsson, M., & Stein, R. F. 1997, ApJ, 481, 500 (CS1997)

Carlsson, M., & Stein, R. F. 1998, in New Eyes to See Inside the Sun and Stars, ed. F.-L. Deubner, J. Christensen-Dalsgaard, D. Kurtz (Kyoto, Kluwer, Dordrecht), Proc. IAU Symp., 185, 435

Carlsson, M., & Stein, R. F. 1999, in Magnetic Fields and Oscillations, Procs. Third Adv. Solar Physics Euroconf., ed. B. Schmieder, A. Hofmann, & J. Staude, ASP Conf. Ser., 184, 206

Carlsson, M., Judge, P. G., & Wilhelm, K. 1997, ApJ, 486, L63

Cook, J. W., Brueckner, G. E., & Bartoe, J.-D. F. 1983, ApJ, 270, L89

Cram, L. E. 1972, Sol. Phys., 22, 375

Cram, L. E. 1978, A&A, 70, 345

Cram, L. E., & Damé, L. 1983, ApJ, 272, 355

Cuntz, M., Rammacher, W., Ulmschneider, P., Musielak, Z. E., & Saar, S. H. 1999, ApJ, 522, 1053

Curdt, W., & Heinzel, P. 1998, ApJ, 503, L95

Curdt, W., Heinzel, P., Schmidt, W., et al. 1999, in Magnetic Fields and Solar Processes, Proc. 9th European Meeting on Solar Physics, ed. A. Wilson, ESA SP-448, ESA Publ. Div., ESTEC, Noordwijk, 177

Damé, L., Foing, B., Martić, M., et al. 1986, Adv. Spac. Res., 6, 273

Deubner, F.-L. 1990, in The Solar Photosphere: Structure, Convection and Magnetic Fields, ed. J.-O. Stenflo (Kiev, Kluwer, Dordrecht), Proc. IAU Symp., 138, 217

Deubner, F.-L. 1998, in New Eyes to See Inside the Sun and Stars, ed. F.-L. Deubner, J. Christensen-Dalsgaard, & D. Kurtz (Kyoto, Kluwer, Dordrecht), Proc. IAU Symp., 185, 427

Deubner, F.-L., & Fleck, B. 1989, A&A, 213, 423

Deubner, F.-L., & Fleck, B. 1990, A&A, 228, 506

Deubner, F. L., & Gough, D. 1984, ARA&A, 22, 593

Deubner, F.-L., & Steffens, S. 1999, in Magnetic Fields and Solar Processes, Procs. 9th European Meeting on Solar Physics, ed. A. Wilson, ESA SP-448, ESA Publ. Div., ESTEC, Noordwijk, 149

Deubner, F.-L., Endler, F., & Staiger, J. 1984, Mem. Soc. Astron. Italia, 55, 135

Deubner, F. L., Fleck, B., Schmitz, F., & Straus, T. 1992, A&A, 266, 560

Deubner, F. L., Waldschik, T., & Steffens, S. 1996, A&A, 307, 936

Doyle, J. G., van den Oord, G. H. J., O'Shea, E., & Banerjee, D. 1999, A&A, 347, 335

Duvall, T. L. 1982, nature, 300, 242

Duvall, T. L., Jefferies, S. M., Harvey, J. W., & Pomerantz, M. A. 1993, Nature, 362, 430

Edmonds, F. N., & Webb, C. J. 1972, Sol. Phys., 22, 276

Endler, F., & Deubner, F. L. 1983, A&A, 121, 291

Foing, B., & Bonnet, R. M. 1984a, A&A, 136, 133

Foing, B., & Bonnet, R. M. 1984b, ApJ, 279, 848

Foing, B., Bonnet, R.-M., & Bruner, M. 1986, A&A, 162, 292

Fontenla, J. M., Avrett, E. H., & Loeser, R. 1993, ApJ, 406, 319

Georgobiani, D., Kosovichev, A. G., Nigam, R., Nordlund, Å., & Stein, R. F. 2000, ApJ, 530, L139

Giovanelli, R. G. 1980, Sol. Phys., 68, 49

Giovanelli, R. G., & Jones, H. P. 1982, Sol. Phys., 79, 267

Goode, P. R., Strous, L. H., Rimmele, T. R., & Stebbins, R. T. 1998, ApJ, 495, L27

Goodman, M. L. 2000, ApJ, 533, 501

Gouttebroze, P., Vial, J. C., Bocchialini, K., Lemaire, P., & Leibacher, J. W. 1999, Sol. Phys., 184, 253

Hagenaar, H. J., Schrijver, C. J., & Title, A. M. 1997, ApJ, 481, 988

Handy, B. N., Acton, L. W., Kankelborg, C. C., et al. 1999, Sol. Phys., 187, 229

Handy, B. N., Bruner, M. E., Tarbell, T. D., et al. 1998, Sol. Phys., 183, 29

Hasan, S. S., & Kalkofen, W. 1999, ApJ, 519, 899

Hindman, B. W., & Brown, T. M. 1998, ApJ, 504, 1029

Hoekzema, N. M., & Brandt, P. N. 2000, A&A, 353, 389

Hoekzema, N. M., & Rutten, R. J. 1998, A&A, 329, 725

Hoekzema, N. M., Brandt, P. N., & Rutten, R. J. 1998a, A&A, 333, 322

Hoekzema, N. M., Rutten, R. J., Brandt, P. N., & Shine, R. A. 1998b, A&A, 329, 276

Hoekzema, N. M., Rutten, R. J., & Cook, J. W. 1997, ApJ, 474, 518

Jefferies, S. M. 1998, in New Eyes to See Inside the Sun and Stars, ed. F.-L. Deubner, J. Christensen-Dalsgaard, & D. Kurtz (Kyoto, Kluwer, Dordrecht), Proc. IAU Symp., 185, 415

Jefferies, S. M., Osaki, Y., Shibahashi, H., et al. 1997, ApJ, 485, L49

Jensen, E., & Orrall, F. Q. 1963, PASP, 75, 162

Jones, H. P., & Giovanelli, R. G. 1983, Sol. Phys., 87, 37

Judge, P. G., & Peter, H. 1998, in Solar Composition and its Evolution – from Core to Corona, ed. C. Fröhlich, M. C. E. Huber, S. Solanki, & R. von Steiger, Procs. ISSI Workshop, Space Sci. Rev., 85, 187

Judge, P. G., Tarbell, T. D., & Wilhelm, K. 2001, ApJ, 554, 424

Kalkofen, W. 1997, ApJ, 486, L145

Kalkofen, W. 1999, in Magnetic Fields and Oscillations, ed. B. Schmieder, A. Hofmann, & J. Staude, Procs. Third Adv. Solar Physics Euroconf., ASP Conf. Ser., 184, 227

Kalkofen, W., Ulmschneider, P., & Avrett, E. H. 1999, ApJ, 521, L141

Kiefer, M., & Balthasar, H. 1998, A&A, 335, L73

Kneer, F., & von Uexküll, M. 1985, A&A, 144, 443

Kneer, F., & von Uexküll, M. 1986, A&A, 155, 178

Kneer F., & von Uexküll M. 1993, A&A, 274, 584

Komm, R., Mattig, W., & Nesis, A. 1991, A&A, 252, 827

Kopp, G., Lindsey, C., Roellig, T. L., et al. 1992, ApJ, 388, 203

Kumar, P. 1994, ApJ, 428, 827

Kumar, P., Fardal, M. A., Jefferies, S. M., et al. 1994, ApJ, 422, L29

Leahy, D. A., Darbro, W., Elsner, R. F., et al. 1983, ApJ, 266, 160

Lites, B. W., & Chipman, E. G. 1979, ApJ, 231, 570

Lites, B. W., Chipman, E. G., & White, O. R. 1982, ApJ, 253, 367

Lites, B. W., Rutten, R. J., & Berger, T. E. 1999, ApJ, 517, 1013

Lites, B. W., Rutten, R. J., & Kalkofen, W. 1993, ApJ, 414, 345 (Paper I)

Lites, B. W., Rutten, R. J., & Thomas, J. H. 1994, in Solar Surface Magnetism, ed. R. J. Rutten, & C. J. Schrijver (Kluwer, Dordrecht), NATO ASI Ser., C 433, 159

Lites, B. W., Thomas, J. H., Bogdan, T. J., & Cally, P. S. 1998, ApJ, 497, 464

Liu, S. Y., & Sheeley, N. R. 1971, Sol. Phys., 20, 282

Liu, S.-Y., & Skumanich, A. 1974, Sol. Phys., 38, 105

Martić, M., & Damé, L. 1989, in Solar and Stellar Granulation, ed. R. J. Rutten, & G. Severino (Kluwer, Dordrecht), NATO ASI Ser., C 263, 207

McIntosh, S. W., Bogdan, T. J., Cally, P. S., et al. 2001, ApJ, 548, L237

Mihalas, B. W., & Toomre, J. 1981, ApJ, 249, 349

Mihalas, B. W., & Toomre, J. 1982, ApJ, 263, 386

Muller, R., Hulot, J. C., & Roudier, T. 1989, Sol. Phys., 119, 229

Musielak, Z. E., Rosner, R., Stein, R. F., & Ulmschneider, P. 1994, ApJ, 423, 474

Neckel, H. 1999, Sol. Phys., 184, 421

Nigam, R., & Kosovichev, A. G. 1999a, ApJ, 510, L149

Nigam, R., & Kosovichev, A. G. 1999b, ApJ, 514, L53

Oliviero, M., Severino, G., Straus, T., Jefferies, S. M., & Appourchaux, T. 1999, ApJ, 516, L45

Rast, M. P. 1999, ApJ, 524, 462

Rutten, R. J. 1988, in Physics of Formation of FeII Lines Outside LTE, ed. R. Viotti, A. Vittone, & M. Friedjung (Reidel, Dordrecht), IAU Coll., 94, 185

Rutten, R. J. 1994, in Chromospheric Dynamics, Proc. Miniworkshop, Inst. Theor. Astrophys., ed. M. Carlsson, Oslo, 25

Rutten, R. J. 1995, in ed. Helioseismology, J. T. Hoeksema, V. Domingo, B. Fleck, & B. Battrick, Proc. Fourth SOHO Workshop, ESA SP–376 vol. 1 (ESA Publ. Div., ESTEC, Noordwijk), 151

Rutten, R. J. 1997, in Advances in the Physics of Sunspots, ed. B. Schmieder, J. C. del Toro Iniesta, & M. Vázquez, Procs. First Adv. in Sol. Phys. Euroconf., ASP Conf. Ser., 118, 298

Rutten, R. J. 1999, in Magnetic Fields and Oscillations, ed. B. Schmieder, A. Hofmann, & J. Staude, Procs. Third Adv. in Sol. Phys. Euroconf., ASP Conf. Ser., 184, 181

Rutten, R. J. 2000, Radiative Transfer in Stellar Atmospheres, Lecture Notes Utrecht University, 7th WWW Edition

Rutten, R. J. 2001, in Cool Stars, Stellar Systems and the Sun, ed. R. J. García Lopez, R. Rebolo, & M. R. Zapatero Osorio, Procs. 11th Cambridge Workshop, ASP Conf. Ser., 223, 117

Rutten, R. J., & Uitenbroek, H. 1991a, Sol. Phys., 134, 15

Rutten, R. J., & Uitenbroek, H. 1991b, in Mechanisms of Chromospheric and Coronal Heating, ed. P. Ulmschneider, E. R. Priest, & R. Rosner, Proc. Heidelberg Conf. (Springer Verlag, Berlin), 48

Rutten, R. J., de Pontieu, B., & Lites, B. W. 1999a, in High Resolution Solar Physics: Theory, Observations, and Techniques, ed. T. R. Rimmele, K. S. Balasubramaniam, & R. R. Radick, Procs. 19th NSO/Sacramento Peak Summer Workshop, ASP Conf. Ser., 183, 383

Rutten, R. J., Lites, B. W., Berger, T. E., & Shine, R. A. 1999b, in Solar and Stellar Activity: Similarities and Differences, ed. C. J. Butler, & J. G. Doyle, Procs. Armagh Workshop, ASP Conf. Ser., 158, 249

Schmieder, B. 1976, Sol. Phys., 47, 435

Schmieder, B. 1977, Sol. Phys., 54, 269

Schmieder, B. 1978, Sol. Phys., 57, 245

Schmitz, F., & Steffens, S. 1999, A&A, 344, 973

Schrijver, C. J., Title, A. M., Berger, T. E., et al. 1999, Sol. Phys. 187, 261

Shine, R. A., & Linsky, J. L. 1974, Sol. Phys., 39, 49

Skartlien, R. 1998, Ph.D. Thesis, Inst. Theor. Astrophys., Oslo (1998)

Skartlien, R., & Rast, M. P. 2000, ApJ, 535, 464

Skartlien, R., Carlsson, M., & Stein, R. F. 1994, in Chromospheric Dynamics, ed. M. Carlsson, Proc. Miniworkshop, Inst. Theor. Astrophys., Oslo, 79

Skartlien, R., Stein, R. F., & Nordlund, Å. 2000, ApJ, 541, 468

Solanki, S. K., & Brigljevic, V. 1992, A&A, 262, L29

Solanki, S. K., & Steiner, O. 1990, A&A, 234, 519

Spruit, H. C. 1976, Sol. Phys., 50, 269

Steffens, S., Deubner, F.-L., Fleck, B., et al. 1997, in Advances in the physics of sunspots, ed. B. Schmieder, J. C. del Toro Iniesta, & M. Vázquez, Procs. First Adv. in Solar Physics Euroconf., ASP Conf. Ser., 118, 284

Stein, R. F., & Carlsson, M. 1997, in SCORe'96: Solar Convection and Oscillations and their Relationship, 261

Stix, M. 2000, Sol. Phys., 196, 19

Straus, T., & Bonaccini, D. 1997, A&A, 324, 704

Straus, T., Severino, G., Deubner, F. L., et al. 1999, ApJ, 516, 939

Theurer, J., Ulmschneider, P., & Cuntz, M. 1997a, A&A, 324, 587

Theurer, J., Ulmschneider, P., & Kalkofen, W. 1997b, A&A 324, 717

Thomas, J. H., & Stanchfield, D. C. H. 2000, ApJ, 537, 1086

Title, A. M., & Berger, T. E. 1996, ApJ, 463, 797

Toner, C. G., & LaBonte, B. J. 1991, ApJ, 415, 847

Uitenbroek, H. 1989, A&A, 213, 360

Ulmschneider, P. 1999, in Solar and Stellar Activity: Similarities and Differences, ed. C. Butler, & J. Doyle, Procs. Armagh Workshop, ASP Conf. Ser., 158, 260

van der Klis, M. 1989, in Timing Neutron Stars, ed. H. Ögelman, & E. P. J. van den Heuvel (Kluwer, Dordrecht), NATO ASI C262, 27

Vernazza, J. E., Avrett, E. H., & Loeser, R. 1973, ApJ, 184, 605

Vernazza, J. E., Avrett, E. H., & Loeser, R. 1976, ApJS, 30, 1

Vernazza, J. E., Avrett, E. H., & Loeser, R. 1981, ApJS, 45, 635

von Uexküll, M., & Kneer, F. 1995, A&A, 294, 252

Vorontsov, S. V., Jefferies, S. M., Duval, T. L. J., & Harvey, J. W. 1998, MNRAS, 298, 464

Wikstøl, Ø., Hansteen, V. H., Carlsson, M., & Judge, P. G. 2000, ApJ, 531, 1150

Worden, J., Harvey, J., & Shine, R. 1999, ApJ, 523, 450